Monthly Notices
of the
ROYAL ASTRONOMICAL SOCIETY

MNRAS **430,** 2739–2754 (2013) doi:10.1093/mnras/stt078

The host-galaxy response to the afterglow of GRB 100901A⋆

Olga E. Hartoog,[1,2†] Klaas Wiersema,[3] Paul M. Vreeswijk,[4] Lex Kaper,[1] Nial R. Tanvir,[3] Sandra Savaglio,[5] Edo Berger,[6] Ryan Chornock,[5] Stefano Covino,[7] Valerio D'Elia,[8,9] Hector Flores,[10] Johan P. U. Fynbo,[11] Paolo Goldoni,[12] Andreja Gomboc,[13,14] Andrea Melandri,[7,15] Alexei Pozanenko,[16] Joop Schaye,[2] Antonio de Ugarte Postigo[17] and Ralph A. M. J. Wijers[1]

[1]*Astronomical Institute Anton Pannekoek, University of Amsterdam, PO Box 94249, NL-1090 GE Amsterdam, the Netherlands*
[2]*Leiden Observatory, Leiden University, PO Box 9513, NL-2300 RA Leiden, the Netherlands*
[3]*Department of Physics and Astronomy, University of Leicester, University Road, Leicester LE1 7RH, UK*
[4]*Centre for Astrophysics and Cosmology, Science Institute, University of Iceland, Dunhaga 5, IS-107 Reykjavik, Iceland*
[5]*Max Planck Institute for Extraterrestrial Physics, D-85748 Garching bei München, Germany*
[6]*Harvard–Smithsonian Center for Astrophysics, 60 Garden Street, Cambridge, MA 02138, USA*
[7]*INAF – Osservatorio Astronomico di Brera, Via E. Bianchi 46, I-23807 Merate (LC), Italy*
[8]*INAF – Osservatorio Astronomico di Roma, Via Frascati 33, I-00040 Monteporzio Catone, Italy*
[9]*ASI Science Data Centre, Via Galileo Galilei, I-00044 Frascati, Italy*
[10]*Laboratoire GEPI, Observatoire de Paris, CNRS-UMR8111, Univ Paris Diderot, 5 place Jules Janssen, F-92195 Meudon, France*
[11]*Dark Cosmology Centre, Niels Bohr Institute, University of Copenhagen, Juliane Maries Vej 30, DK-2100 Copenhagen, Denmark*
[12]*APC, Astroparticules et Cosmologie, Universite Paris Diderot, CNRS/IN2P3, CEA/Irfu, Observatoire de Paris, Sorbonne Paris Cite, 10, rue Alice Domon et Leonie Duquet, F-75205 Paris Cedex 13, France*
[13]*Faculty of Mathematics and Physics, University of Ljubljana, Jadranska 19, SI-1000 Ljubljana, Slovenia*
[14]*Centre of Excellence SPACE-SI, Aškerčeva cesta 12, SI-1000 Ljubljana, Slovenia*
[15]*Astrophysics Research Institute, Liverpool John Moores University, Twelve Quays House, Egerton Wharf, Birkenhead, CH41 1LD, United Kingdom*
[16]*Space Research Institute (IKI), 8432 Profsoyuznaya str., 117997 Moscow, Russia*
[17]*Instituto de Astrofísica de Andalucía (IAA-CSIC), Glorieta de la Astronomía s/n, E-18008 Granada, Spain*

Accepted 2013 January 10. Received 2013 January 4; in original form 2012 July 20

ABSTRACT

For gamma-ray burst 100901A, we have obtained Gemini-North and Very Large Telescope optical afterglow spectra at four epochs: 1 h, 1 d, 3 d and 1 week after the burst, thanks to the afterglow remaining unusually bright at late times. Apart from a wealth of metal resonance lines, we also detect lines arising from fine-structure levels of the ground state of Fe II, and from metastable levels of Fe II and Ni II at the host redshift ($z = 1.4084$). These lines are found to vary significantly in time. The combination of the data and modelling results shows that we detect the fall of the Ni II $^4F_{9/2}$ metastable level population, which to date has not been observed. Assuming that the population of the excited states is due to the ultraviolet radiation of the afterglow, we estimate an absorber distance of a few hundred pc. This appears to be a typical value when compared to similar studies. We detect two intervening absorbers ($z = 1.3147, 1.3179$). Despite the wide temporal range of the data, we do not see significant variation in the absorption lines of these two intervening systems.

Key words: gamma-ray burst: individual: GRB 100901A – galaxies: abundances – galaxies: distances and redshifts – galaxies: ISM.

1 INTRODUCTION

Shortly after the first detection of an optical afterglow associated with a long gamma-ray burst (GRB; van Paradijs et al. 1997), it became clear that GRBs may be useful probes of distant galaxies: afterglows can be very bright and have a simple power-law continuum at ultraviolet (UV) to optical wavelengths, against which

⋆ Based on observations obtained at the Gemini Observatory at Mauna Kea under programme GN-2010B-Q-7, and observations obtained with European Southern Observatory (ESO) Telescopes at the Paranal Observatory under programme 085.A-0009(B).

† E-mail: O.E.Hartoog@uva.nl

otherwise undetectable absorbing systems, such as the gas in the host galaxy, leave an observable signature (see e.g. Vreeswijk et al. 2001, 2004; Savaglio, Fall & Fiore 2003; Berger et al. 2006; Fynbo et al. 2006; Prochaska et al. 2007). Long GRBs are formed as end products of the evolution of massive stars (Woosley 1993; Paczyński 1998) and should therefore probe star-forming regions. Their optical afterglows fade away on short time-scales (∼days), making it possible to study their host galaxies in emission as well (see e.g. Savaglio, Glazebrook & Le Borgne 2009; Hjorth et al. 2012). For a review of long GRBs and their host galaxies, see e.g. Savaglio (2006, 2012).

Optical spectra (i.e. rest-frame UV at redshifts around $z \sim 1$–2) of GRB afterglows generally show strong absorption lines of metals, both at low- and high-ionization stages, as well as high neutral hydrogen column densities (see Fynbo et al. 2009 for a large and relatively unbiased sample). Absorption lines provide the redshift and allow estimation of column densities of the host galaxy of the GRB and possibly other absorbers along the line of sight. This provides valuable information on the metallicity and dust content of galaxies at an arbitrary redshift, regardless of the brightness of these systems, which is very difficult to obtain otherwise. The highest redshift lines in the afterglow spectrum formally only provide a lower limit on the host redshift. However, the presence of fine-structure lines can confirm the galaxy as the host, because these arise from excited states that are expected to have been populated by the UV afterglow radiation of the GRB (Prochaska, Chen & Bloom 2006; Vreeswijk et al. 2007). These lines are not seen in foreground line-of-sight absorbers in quasar (QSO) spectra, except for some relatively low-energy excited states from carbon. Due to the transient nature of the afterglow, the absorption lines from these excited states are expected to vary in strength, which may provide information on the internal distribution of gas and kinematics within the host galaxy, often the only way to obtain such information for these distant and mostly faint galaxies. Fine-structure line variation has been measured and modelled for a handful of bursts (e.g. Dessauges-Zavadsky et al. 2006; Vreeswijk et al. 2007, 2013; D'Elia et al. 2009a; Ledoux et al. 2009; de Ugarte Postigo et al. 2011; De Cia et al. 2012), which allowed constraints to be placed on the distance between the burst and the absorbing material (see Vreeswijk et al. 2013 for a description of the methods used).

The primary difficulty in probing column density variations in GRB sight lines to fit to the models described above is the requirement of afterglow brightness: for fainter afterglows the necessary high signal-to-noise ratio (S/N) and high spectral resolution are difficult to obtain with current instrumentation. This also limits this method to early-time data and a limited range of instruments, making it difficult to build up a sample. In the cases described above, the variation is measured with high-resolution spectrographs, and all spectra are obtained within a few hours post burst (observer's frame).

The optical afterglow of GRB 100901A remained unusually bright out to very late times, which allowed us to collect spectra over a time span of a week with the Gemini-North Multi-Object Spectrograph and X-shooter on the ESO Very Large Telescope (VLT). In this paper, we investigate the behaviour of the excited level populations over this unusually long time span, and the application of the excitation models to low- and intermediate-resolution spectra. The observations and data reduction are described in Section 2. We study the metal resonance lines at the host-galaxy redshift in Section 3.1. In Section 3.1.1, we examine the dust content of the host galaxy. The two intervening absorbers are analysed in Section 3.1.3. In Section 3.2, the fine-structure line variability is described and modelled. In Section 3.3, we briefly discuss the emission lines from the host galaxy. We discuss our results in Section 4 and summarize our conclusions in Section 5.

Throughout the paper we adopt a standard Λ cold dark matter cosmology with $H_0 = 71\,\mathrm{km\,s^{-1}\,Mpc^{-1}}$, $\Omega_\mathrm{m} = 0.27$ and $\Omega_\Lambda = 0.73$. We indicate line transitions by their vacuum wavelengths.

2 OBSERVATIONS

GRB 100901A was detected by *Swift* on 2010 September 1 at 13:34:10 UT. With a total duration of $T_{90} = 439 \pm 33$ s (Immler et al. 2010; Sakamoto et al. 2010) the burst is clearly classified as a long burst. The optical afterglow candidate at RA (J2000) = $01^\mathrm{h}\,49^\mathrm{m}\,03\overset{\mathrm{s}}{.}42$, Dec. = $+22^\circ\,45'\,30\overset{''}{.}8$ (90 per cent confidence error radius of about 0.81 arcsec) was identified in an Ultraviolet/Optical Telescope (UVOT) exposure which started 147 s after the Burst Alert Telescope (BAT) trigger (Immler et al. 2010). Automatic observations with the Faulkes Telescope North identified an uncatalogued object at the position consistent with the UVOT candidate (Guidorzi et al. 2010). Several follow-up photometry efforts followed, resulting in the light curve presented and analysed in Gomboc et al. (in preparation) and Gorbovskoy et al. (2012) (see also Fig. 8). The first optical spectrum of the afterglow was taken with the Gemini Multi-Object Spectrograph (GMOS) on Gemini-North (programme GN-2010B-Q-7, PI Tanvir), approximately 1 h 15 min (0.0526 d) after burst trigger (Chornock et al. 2010). With this instrument, two other spectra at, respectively, 1 and 7 d after the burst were obtained. A fourth spectrum was obtained approximately 3 d after the burst with the X-shooter spectrograph mounted on the ESO VLT, under programme 085.A-0009(B) (PI Fynbo). See Table 1 for a detailed log of the observations presented in this paper.

2.1 Gemini-N/GMOS spectroscopy

Gemini-N/GMOS is a low-resolution long-slit spectrograph, equipped with three detectors. For the observations presented here, a slit width of 0.75 arcsec and the B600 grism with the G5307 order suppression filter have been used, which resulted in the wavelength coverage and resolving power reported in Table 1. We used four exposures per epoch, using dithers in both dispersion and spatial coordinates to sample over the chip gaps and regions affected by amplifier location. The GMOS spectra have been reduced with the IRAF packages for Gemini GMOS (version 1.9), using arc line exposures taken directly before and after the science data. The four exposures are combined after extraction. The resulting spectra were normalized and no flux calibration was performed.

2.2 VLT/X-shooter spectroscopy

VLT/X-shooter is a cross-dispersed échelle spectrograph where the incoming light is split into three wavelength arms using dichroics, covering the full optical to near-infrared (NIR) wavelength range simultaneously (D'Odorico et al. 2006; Vernet et al. 2011). The X-shooter spectra have been taken in nodding mode with 1×2 binning (i.e. binning in the dispersion direction) in the UV-Blue (UVB) and Visual (VIS) arms, using a 100 kHz/high-gain readout and 4×600 s exposure times. The selected slit widths were 1.0, 0.9 and 0.9 arcsec for the UVB, VIS and NIR arms, respectively. A 5 arcsec nod throw along the slit was used to improve sky subtraction. The spectra were reduced using the ESO pipeline software version 1.2.2, using the so-called physical model mode (Goldoni et al. 2006; Modigliani

Table 1. Overview of the spectroscopic observations of the afterglow of GRB 100901A, arranged by instrument and epoch. Columns (1) and (2) indicate telescope, instrument, setup and slit dimensions. Column (3) gives the wavelength coverage for this setup and the resolving power $R = \lambda/\Delta\lambda$, with $\Delta\lambda$ the FWHM of an unresolved line. Column (4) gives the mid-time of the epochs of observation in days after the burst BAT trigger. Column (5) lists the interpolated observed R magnitude of the afterglow at this epoch (Gomboc et al., in preparation). Column (6) lists the total exposure time of the observation in this epoch. Columns (7) and (8) give the seeing and the airmass. The seeing is measured by fitting a Gaussian along the spatial direction of the slit, around the central wavelength of each spectrum. Column (9) gives the S/N in the continuum at 4150 and 6100 Å per GMOS pixel ($\delta\lambda = 0.91$ Å). Column (10) gives the name we will use to refer to the epoch.

Telescope	Instrument and setup	Spectral range and resolution	Time after burst (d)	m_R	Exp. time (s)	Seeing (arcsec)	Airmass	S/N/($\delta\lambda = 0.91$ Å) at 4150, 6100 Å	Abbrev.
Gemini-North	GMOS,	3810−6710 Å	0.0526	17.8	4 × 400	0.62	1.06	38, 95	epoch1
	B600+ G5307	$R = 1000-1900$	1.0095	18.6	4 × 500	0.52	1.01	16, 70	epoch2
	0.75 arcsec × 330 arcsec		7.0270	22.3	4 × 1200	0.68	1.05	5, 13	epoch3
Very Large	X-shooter	3000−25000 Å	2.7492	20.2	4 × 600	1.30	1.48	9, 7	xsh
Telescope	UVB 1.0 arcsec × 11 arcsec	$R = 5400$							
	VIS 0.9 arcsec × 11 arcsec	$R = 7400$							
	NIR 0.9 arcsec × 11 arcsec	$R = 5800$							

et al. 2010). We used calibration data (bias, dark, arc-lamp, flat-field and flexure control frames) taken the next day or as close in time as possible to the science observations. The bin sizes of the resulting spectra were 0.2, 0.2 and 0.5 Å for UVB, VIS and NIR spectra, respectively. Extracted spectra were flux calibrated using spectrophotometric standard star exposures, also taken the same night, resulting in roughly flux-calibrated spectra spanning the near-UV to the NIR. We caution that the weather conditions during this night were poor, and likely non-photometric. We used a telluric standard star (HD 4670, a B9 V star) to correct the telluric absorption features in the NIR afterglow spectrum, using the IDL SPEXTOOL package (Vacca, Cushing & Rayner 2003, see also Wiersema 2011 for the use on X-shooter data).

3 ANALYSIS

The GMOS epoch1 spectrum (see Fig. 1) is that of a bright afterglow including many metal absorption lines. At a redshift of 1.4084 we detect strong resonance lines of Fe II, Mn II, Cr II, Al II, Al III, Zn II and Si II. Additionally, at the same redshift, line transitions arising from excited states of Fe II and Ni II are clearly detected (see Section 3.2). Therefore, we identify this as the host-galaxy redshift z_h (Chornock et al. 2010). We do not detect lines from Fe III, as observed in the case of GRB 080310 (De Cia et al. 2012). No Lyman α is detected, because it is too far in the blue for the covered wavelength range. Two intervening absorbers are visible at $z_1 = 1.3147$ and $z_2 = 1.3179$ (Chornock et al. 2010). In these systems we detect Fe II, Al II, Al III, Mg I and Mg II (rest-frame equivalent width $W_\lambda < 1$ Å). We note that these lines are weaker at the intervening system redshifts than at the host redshift. There are no fine-structure lines detected at any of the intervening absorber redshifts. Na I λλ 5892, 5898 are detected at $z = 0$ and are thus due to foreground absorption in the Galaxy.

The GMOS epoch2 spectrum (not fully shown in a figure) looks similar, though the S/N is lower due to the decreasing brightness of the afterglow. The line transitions arising from the metastable Ni II $^4F_{9/2}$ level (see Table A4) appear more pronounced in epoch2 than in epoch1; the Fe II fine-structure lines have become slightly weaker.

Since GMOS epoch3 is observed after the break in the light curve at ∼2 d (Gomboc et al., in preparation), which causes the brightness to drop more quickly, the S/N is lower than for the other epochs, despite the longer integration time and comparable weather conditions. Still, strong metal resonance lines are clearly detected. Fine-structure lines that were present in epoch1 and lines from metastable levels that were present in epoch2 are much weaker or not detected any more (see Section 3.2).

The quality of the X-shooter spectrum (xsh, after 2.75 d, see Table 1) is low due to poor weather conditions and large airmass, but because of the extraordinarily large wavelength coverage of this instrument, this spectrum does provide additional information. Moreover, the higher resolution allows us to exclude the existence of different velocity components down to ∼70 km s^{-1} with respect to ∼200 km s^{-1} for GMOS. The strong and saturated Mg II λλ 2796, 2803, Mg I λ 2853 and Ca II λλ 3934, 3969 absorption lines from the host galaxy are outside the range of GMOS due to the redshift, but they are clearly detected in xsh-VIS (not shown in a figure). Na I λ 5892, 5897 falls in a region with atmospheric absorption and can therefore not be detected. We do not detect the red wing of the Lyman α absorption line due to low S/N. Furthermore, in xsh-NIR, we marginally detect forbidden oxygen emission line [O III] λ5007 at the host-galaxy redshift (see Fig. 9 and Section 3.3).

We do not detect prominent interstellar (dust) extinction features such as the 2175 Å feature (see e.g. Elíasdóttir et al. 2009) or diffuse interstellar bands in any of the spectra at the host-galaxy redshift.

3.1 Resonance lines

To measure the observed equivalent width $W_{\lambda,\,\mathrm{obs}}$ of the absorption lines in the spectrum, we locally fit Gaussian functions to the normalized spectrum with NGAUSSFIT, a task in the STSDAS package in IRAF. In principle, $W_{\lambda,\,\mathrm{obs}}$ can be obtained directly by integration, but as can be seen in Fig. 1, many lines are blended. In some cases, one line needs to be fixed in order to measure the potential variation of the other. NGAUSSFIT can deblend up to three lines, with the possibility to keep part of the parameters fixed. This method allows that in spectra with low S/N, an absent or very weak line is sometimes formally best fitted with a line with negative equivalent width (i.e. an emission line; see also Figs 6 and 7); for these lines we obtain upper limits for $W_{\lambda,\,\mathrm{obs}}$.

The formal error on the equivalent width is obtained from the error spectrum

$$\sigma(W_{\lambda,\mathrm{obs}}) = \delta\lambda \sqrt{\sum_{i}^{\mathrm{line}} (\sigma_i / F_c)^2}, \quad (1)$$

with $\delta\lambda$ the spectral bin width, σ_i the value of the error spectrum in bin i and F_c the continuum flux. The summation runs over two times the full width at half-maximum (FWHM). Furthermore, we

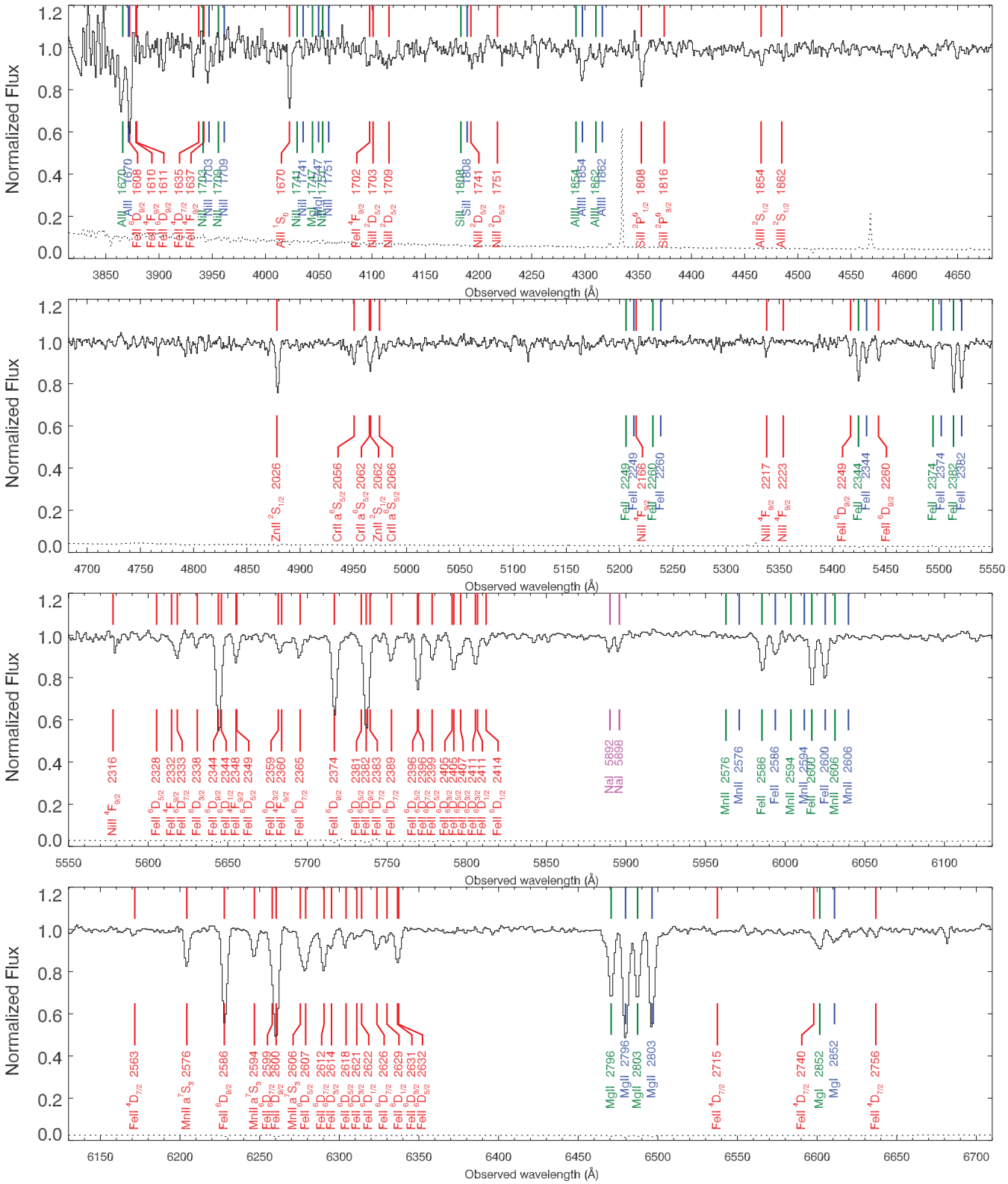

Figure 1. Normalized GMOS spectrum (epoch1) of the afterglow of GRB 100901A. The red labels indicate the absorption lines of the host ($z_h = 1.4084$); the green and blue labels (with a vertical offset) indicate the absorption lines formed in two intervening systems at $z_1 = 1.3147$ and $z_2 = 1.3179$. The magenta labels show unshifted Na I lines ($z = 0$), resulting from the absorption in the Milky Way. The numbers at the labels indicate the configuration of the lower level and the vacuum rest wavelength of the transition. The host shows resonance lines from the ions Mn II, Fe II, Cr II, Zn II, Si II, Al II and Al III, as well as lines from the excited states of Fe II and Ni II, which are found to vary significantly (see Section 3.2). In the intervening systems we detect Mg I, Mg II, Fe II, Al II and Al III.

Table 2. The measured rest-frame equivalent width W_λ for the resonance lines at the host redshift, and the corresponding ion column densities, obtained with curve-of-growth (COG) analysis. The first column lists the ion and the vacuum rest wavelength (Å); the second column gives the oscillator strength f_λ. Columns (3) and (4) give the rest-frame W_λ in Å measured in epoch1 and epoch2 (GMOS), respectively. For lines for which we have a good measurement both in epoch1 and epoch2, the weighted average is used; otherwise we use the value measured in epoch1. The values that are finally used for the COG analysis are listed in Column (5). Column (6) gives the best-fitting column density for the ion, fitted to a COG with effective Doppler parameter $b = 22.1^{+1.7}_{-1.6}$ km s^{-1}. Columns (7) and (8) give the relative abundances with respect to iron and zinc using solar values from Asplund et al. (2009) (for notation see equation 2). The references for the wavelength and oscillator strength are given in column (9).

Line	f_λ	W_λ/(Å) epoch1	W_λ/(Å) epoch2	$\langle W_\lambda/\text{Å}\rangle$	$\log(N_{\rm ion}/\text{cm}^{-2})$	[X/Fe]	[X/Zn]	Reference
Al II 1670.7874	1.740	0.418 ± 0.093	0.338 ± 0.098	0.380 ± 0.067	$13.57^{+0.41}_{-0.32}$	-0.61 ± 0.42	-1.84 ± 0.42	1
Al III 1854.7164	5.39×10^{-1}	0.113 ± 0.054	0.162 ± 0.060	0.135 ± 0.040	$13.02^{+0.13}_{-0.16}$	[a]	[a]	1
Al III 1862.7895	2.68×10^{-1}	0.044 ± 0.051	0.113 ± 0.056	0.075 ± 0.038	–			1
Si II 1808.013	2.080×10^{-3}	0.292 ± 0.062	0.267 ± 0.068	0.281 ± 0.046	$15.96^{+0.18}_{-0.16}$	$+0.72 \pm 0.19$	-0.51 ± 0.19	2
Zn II 2026.136[b]	5.010×10^{-1}	0.362 ± 0.046	0.280 ± 0.053	0.327 ± 0.035	$13.52^{+0.07}_{-0.07}$	$+1.23 \pm 0.10$		3
Zn II 2062.664	2.460×10^{-1}	0.191 ± 0.041	0.206 ± 0.048	0.197 ± 0.031	–			3
Cr II 2056.2539	1.030×10^{-1}	0.150 ± 0.040	0.151 ± 0.046	0.151 ± 0.030	$13.73^{+0.09}_{-0.10}$	$+0.36 \pm 0.12$	-0.87 ± 0.12	3
Cr II 2066.161	5.120×10^{-2}	0.096 ± 0.038	0.111 ± 0.045	0.102 ± 0.029	–			3
Fe II 2249.8754[c]	2.190×10^{-3}	0.129 ± 0.034	0.151 ± 0.040	0.139 ± 0.026	$15.23^{+0.07}_{-0.08}$		-1.23 ± 0.10	4
Fe II 2260.7793	2.620×10^{-3}	0.152 ± 0.034	0.168 ± 0.040	0.159 ± 0.026	–			4
Fe II 2586.6495	7.094×10^{-2}	0.705 ± 0.044	0.727 ± 0.048	0.715 ± 0.032	–			4
Mn II 2576.877	3.610×10^{-1}	0.265 ± 0.032	0.257 ± 0.037	0.262 ± 0.024	$13.23^{+0.04}_{-0.05}$	$+0.07 \pm 0.09$	-1.16 ± 0.04	5
Mn II 2594.499	2.800×10^{-1}	0.206 ± 0.030	0.207 ± 0.034	0.207 ± 0.023	–			5
Mn II 2606.462	1.980×10^{-1}	0.164 ± 0.064	[d]	0.164 ± 0.064	–			5
Mg II 2796.352	6.123×10^{-1}			0.920 ± 0.147[e]	$15.06^{+0.83}_{-0.60}$	-0.27 ± 0.83	-1.50 ± 0.83	6
Mg II 2803.531	3.054×10^{-1}			0.918 ± 0.126[e]	–			6
Ca II 3934.777	6.500×10^{-1}			0.907 ± 0.220[e]	$13.74^{+0.47}_{-0.50}$	-0.33 ± 0.50	-1.56 ± 0.50	7
Ca II 3969.591	3.220×10^{-1}			0.836 ± 0.185[e]	–			7

[a]The quantities [Al III/Fe] and [Al III/Zn] do not have any physical meaning, since the Al III is probably mainly from a different region than Al II, Fe II and Zn II (see also Savaglio & Fall 2004).
[b]The contamination by Cr II λ2026 is determined from the other Cr II lines and is negligible. The contribution of Mg I λ2026 cannot be determined, but we assume that it is small based on the absence of Mg I λ1827.
[c]Fe II 2344, 2374, 3282 and 2600 are also clearly detected, but these are blended with fine-structure lines and therefore not used in the abundance study. Estimates of their equivalent widths can be found in Appendix A.
[d]The equivalent width of the line is fixed in the second epoch in order to measure the varied strength of the blended fine-structure line(s).
[e]Absorption lines are outside the GMOS range; measurement is from xsh spectrum.
References for atomic data: (1) NIST Atomic Spectra Database, (2) Bergeson & Lawler (1993b), (3) Bergeson & Lawler (1993a) (4) Verner et al. (1999), (5) Morton (2003), (6) Verner et al. (1996), (7) Morton (1991).

add 3 per cent of the equivalent width to the formal error to account for the uncertainty in placing the continuum. In the low-resolution GMOS spectra, all absorption lines are unresolved and can be fitted with a Gaussian with a fixed FWHM of 3.6 Å (the resolution element), which is determined from the width of the lines in the arc-lamp frames. In xsh we fix FWHM = 1.0 and 0.7 Å in the UVB and VIS arms, respectively, based on the widths of arc lines and telluric emission lines. Some strongly saturated lines (for example, the Mg II doublet) in these spectra cannot be fitted with Gaussians and are therefore integrated numerically. The resulting rest-frame equivalent widths $W_\lambda = W_{\lambda,\rm obs}/(1+z_{\rm h})$ of the resonance lines in the first two epochs are listed in Table 2.

To infer column densities of the different ions from the absorption line equivalent widths, we make use of a multi-ion single-component curve-of-growth (MISC-COG) analysis (Spitzer 1978). The Doppler line width is in principle related to the temperature and the level of turbulence in the absorbing gas. Limited by spectral resolution, it is difficult to distinguish between this and broadening due to the complex physical structure of absorbing clouds in the sight line. Therefore, we speak of an 'effective' Doppler parameter, which does not carry information about the temperature of the gas, but is merely a simplification in the model (Jenkins 1986). The assumption we need to make in this analysis is that the effective Doppler parameter b is the same for all ion species, and that it is single (one velocity component). In other words, we assume that the velocity structure is the same in all lines, and that it is dominated by small-scale effects such as thermal velocities and turbulence and not by differences in bulk velocities of different gas clouds.

3.1.1 *Host-galaxy column densities*

We use three unblended Fe II resonance lines (λ2249, λ2260 and λ2586) to determine b for the line-of-sight gas in the host galaxy (see Table 2). Because these lines cover both the linear and the flat part of the COG, both b and the column density for Fe II, $N_{\rm Fe\,II}$, can be constrained. They are dependent variables; therefore, we fit them simultaneously with a grid method, yielding $b = 22.1^{+1.7}_{-1.6}$ km s^{-1} and $\log N_{\rm Fe\,II}/\text{cm}^{-2} = 15.23^{+0.07}_{-0.08}$.

The COG with the best-fitting value for b is shown in Fig. 2. The ion species other than iron have line transitions either on the linear or on the flat part of the COG; therefore, b has to be assumed

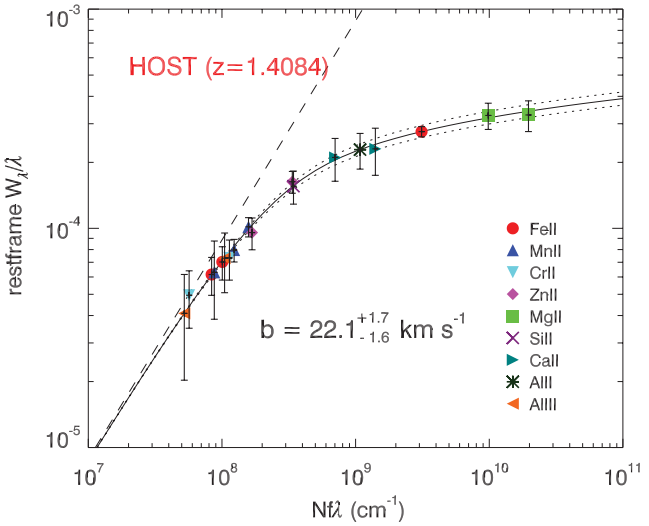

Figure 2. COG for the resonance lines in the host galaxy of GRB 100901A. The solid line gives the best-fitting COG with $b = 22.1\,\mathrm{km\,s^{-1}}$, the dotted lines show the effect of the error on b. The dashed line, which coincides with the linear part of the COG, is a COG for $b = \infty$, that can be used as an approximation for weak lines.

to be the same for all ion species in order to determine the column densities. The resulting column densities of the ions are listed in Table 2. For most lines we have taken an average of the first two epochs, except Mg II and Ca II which can only be measured in xsh. The equivalent widths of the Al II lines are slightly larger in epoch1 while those of Al III are larger in epoch2. While not very significant, it may be a sign of ionization due to the GRB afterglow (see e.g. Vreeswijk et al. 2013). Due to the low significance we decided not to take this into account in the excitation modelling in Section 3.2.

Spectral resolution limits the ability to distinguish different velocity components in absorption lines: an instrumental FWHM = 3.6 Å (GMOS spectra) corresponds to $\sim$200 km s^{-1}. In xsh-VIS, a velocity component difference of $\sim$70 km s^{-1} would be detectable, but we do not see indications for more than one velocity component in any of the lines. This could be due to the low S/N of xsh, because most intermediate- to high-resolution spectra of GRBs show absorption lines with at least two components (but see e.g. Ledoux et al. 2009).

Prochaska (2006) warns that column densities derived with the MISC-COG method are systematically underestimated, especially when the underlying line structure is that of separated clumps of gas at different velocity shifts. In this case, one derives a high b with MISC-COG analysis, and therefore a lower column density. Results for a single-component COG analysis with $b \gtrsim 20\,\mathrm{km\,s^{-1}}$ are highly suspect, according to Prochaska (2006). That COG analysis of a low-resolution spectrum can be accurate is shown by D'Elia et al. (2011), who compare low- and high-resolution spectra for the afterglow of GRB 081008. The COG analysis gives the same result as line fits to the high-resolution spectrum within 3σ. They conclude that this is linked to the low level of saturation of the lines. The equivalent widths of the low-ionization lines in GRB 100901A are found to be in the lowest 10 per cent of the sample of 69 low-resolution spectra conducted by de Ugarte Postigo et al. (2012), which strengthens the case that a COG analysis on this spectrum can provide accurate results. However, column densities resulting from the COG analysis always need to be treated with caution.

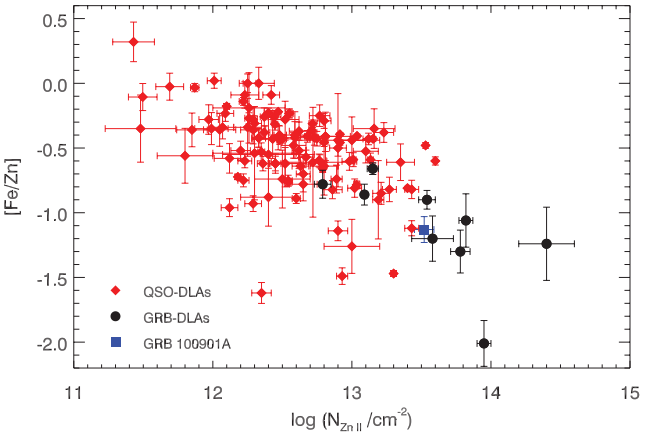

Figure 3. [Fe/Zn] as a function of the Zn II column density in QSO-DLAs (red diamonds), GRB-DLAs (black circles) and GRB 100901A (blue square). QSO-DLA values are from Lu et al. (1996), Prochaska & Wolfe (1996, 1997, 2000), Pettini et al. (1999, 2000) and Prochaska et al. (2001). GRB-DLA values are from Savaglio et al. (2003), Fynbo et al. (2002), Fiore et al. (2005), Watson et al. (2006), Penprase et al. (2006), Vreeswijk et al. (2007) and D'Elia et al. (2009b, 2011).

3.1.2 *Dust depletion*

The strength of the absorption lines in the spectrum is a measure of the abundance of an element in the gas phase only. Apart from the overall gas-to-dust ratio, the fraction of a specific element that is locked on to dust depends on the element species and on the nature of the dust. Therefore, the pattern of relative abundances, the depletion pattern, might give an insight into the amount and nature of the dust. In Table 2 we list the abundance ratios with respect to the refractory (depleted) element Fe and the non-refractory element Zn, compared to the ratio in a solar abundance environment. We use the following, commonly used notation

$$[X/Y] \equiv \log\left(\frac{N(X)}{N(Y)}\right) - \log\left(\frac{n(X)}{n(Y)}\right)_{\odot}, \qquad (2)$$

with $N(X)$ the column density of element X and $n(X)$ the number density of element X in a solar environment (Asplund et al. 2009). Differences from zero indicate dust content. We thus assume that relative abundances (both in gas and dust) are solar. Fe, Zn and Cr are iron peak elements, which makes this a reasonable assumption, although the main production pathway of Zn is not fully identified (Umeda & Nomoto 2002). Discrepancies in relative abundances might also be due to a different star-formation history than the Milky Way (MW).

In Fig. 3 we show [Fe/Zn] as a function of the Zn column density for the host of GRB 100901A, compared with a sample of other GRB-DLAs and QSO-DLAs.[1] The relative abundance values indicate a stronger depletion (i.e. more dust) in GRB-DLAs than in QSO-DLAs, but among the GRB-DLAs, GRB 100901A is not a particularly special case. Both GRB-DLAs and QSO-DLAs appear to follow the overall trend that systems with stronger Zn column densities show stronger depletion. The fact that the two classes populate different regions in the diagram is mainly a sight line effect. QSOs probe galaxies in random orientations with only a small chance that the densest region of a galaxy is intersected,

[1] DLA: damped Lyman α system: a sight line absorber with $N_{\mathrm{H\,I}} > 2 \times 10^{20}$ cm^{-2} (Wolfe, Gawiser & Prochaska 2005). A DLA system in a GRB afterglow spectrum is usually due to the host galaxy.

while sight lines to GRB afterglows probe the gas towards the progenitor region, so they will in general show high column densities (see also Savaglio 2006; Prochaska et al. 2007; Fynbo et al. 2009). Furthermore, for GRB-DLAs with relatively low column densities and weak absorption lines, [Fe/Zn] is not well constrained (i.e. not reported in the literature) because the fading afterglow prevents building up of S/N over several nights of observations. This is not the case for QSO-DLAs, which is why these objects also populate the low $N_{\rm Zn\,II}$ part of the parameter space.

A more detailed analysis of the dust content can be performed by comparing the heavy-element dust depletion pattern of GRB 100901A with observations in the interstellar medium (ISM) of the MW (Savage & Sembach 1996). We use the method described in Savaglio & Fall (2004). We consider the observed depletion patterns in the MW sight lines through a warm halo (WH), warm disc and halo (WDH), warm disc (WD) and cool disc (CD) as models. For the fit, we use two free parameters. One is the dust-to-metal ratio relative to the Galactic values $\kappa = \kappa_{\rm GRB}/\kappa_J$ (J is one of the four depletion patterns). The second is proportional to the metallicity (not known because $N_{\rm H\,I}$ is not measured in GRB 100901A). The two parameters are scaled until they reproduce the observed heavy-element depletion pattern best (minimum χ^2).

Results using measurements of seven elements are shown in Fig. 4. The WH depletion pattern gives the smallest χ^2 among the four patterns, but the WD pattern is also a reasonable fit. The dust-to-metal ratio is between the MW value and 10 per cent higher. Ni and Mg are the most uncertain measurements. The Mg II column density is likely a lower limit because it suffers from very strong saturation. The Ni II column density is not measured from the resonance lines directly, but follows from the modelling of the time evolution of the Ni II $^4F_{9/2}$ metastable level (see Section 3.2.1 and Table 5). Excluding these two elements from the fit does not change our results much.

For the observed column of metals, and assuming a rate of visual extinction per column density of metals like in the MW (Bohlin, Savage & Drake 1978), the expected optical extinction in GRB 100901A would be $A_V \sim 0.5$. This is higher than the one derived from the spectral energy distribution (SED) of GRB 100901A ($A_V = 0.21$; Gomboc et al., in preparation). This inconsistency is typically observed in GRB sight lines (Schady et al. 2011) and indicates that the rate of extinction in the ISM of GRB hosts per column of metals is different from what is observed in the MW.

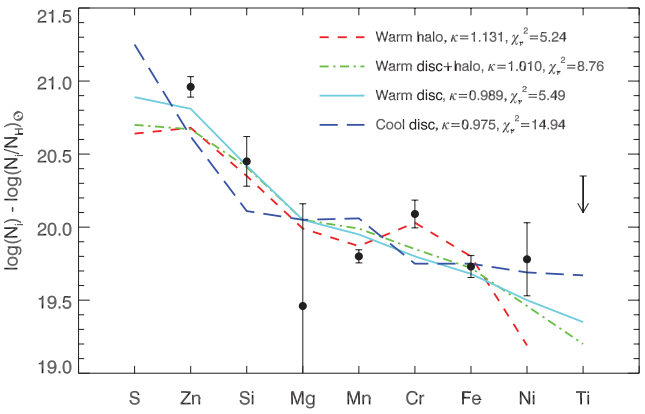

Figure 4. Depletion pattern for the host of GRB 100901A, compared with different components in the MW (Savage & Sembach 1996), which are observed patterns that can be adjusted by changing the dust-to-metal ratio κ. The column density of Ni II is not directly measured but follows from the modelling of the fine-structure and metastable levels, see Section 3.2.1. We include a 3σ upper limit for Ti II based on the absence of the doublet at a rest wavelength of 1910 Å.

3.1.3 *Intervening absorbers*

Two intervening absorbers are detected: int1 at $z_1 = 1.3147$ and int2 at $z_2 = 1.3179$. If these two systems are not physically associated with each other, and the redshift difference is dominated by cosmological expansion, the velocity difference corresponds to a comoving separation of 3.9 Mpc. If the absorbers belong to one system, the velocity difference is 414 km s^{-1}, and could be due to motion of galaxies within a cluster.

Because of the long time span that our observations cover (until long after the jet break; Gomboc et al., in preparation), the data set is suited to look for variations in the strength of the lines from the intervening absorbers. This can be interesting in the context of the previously supposed discrepancy between the number of strong Mg II absorbers ($W_\lambda(2796) > 1$ Å) in QSO and GRB sight lines; in the latter the redshift number density was found to be about two times as high (Prochter et al. 2006; Cucchiara et al. 2009; Vergani et al. 2009). However, Cucchiara et al. (2012) used a larger sample and did not reproduce this discrepancy.

We do not detect variability above the 2σ level in any of the two intervening absorbers of GRB 100901A, and we see no systematic trend in the ensemble of lines per absorber, nor per ion species. In principle, the non-variation of the equivalent widths of the intervening absorber resonance lines gives a lower limit on the

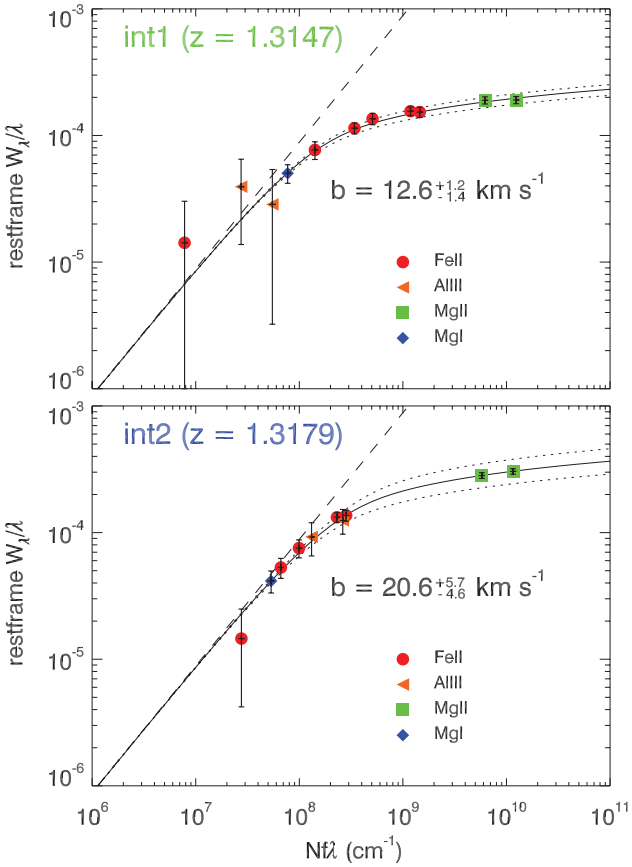

Figure 5. COG for the two intervening systems in the sight line to GRB 100901A. The lines used and the best-fitting column densities are listed in Table 3.

size of the absorbing clouds (i.e. the scale on which the absorbing gas is homogeneous). If the projected apparent size of the afterglow became larger than the projected size of the intervening absorber, the absorption lines from this system would become weaker since part of the light would reach the observer unabsorbed. We use the description of the apparent size of the Blandford–McKee spherical expansion described by Granot, Piran & Sari (1999), where we use $E_{\rm iso} = 6.3 \times 10^{52}$ erg (Gorbovskoy et al. 2012). We assume the close circumburst medium to have a constant density of $n = 1\,{\rm cm}^{-3}$. At the time of the last epoch (7.027 d), we find the source to be 9.6×10^{16} cm. This gives a lower limit on the size of each of the absorbing clouds of 0.03 pc. Although this is not a very meaningful lower size limit for a gas cloud, we point out that in general it is difficult to put limits on absorber sizes, but see D'Elia et al. (2010a) for methods applied to GRB absorbers and Petitjean et al. (2000), Ellison et al. (2004) and Balashev et al. (2011) for examples of size estimates of QSO line-of-sight objects.

Because the lines of the intervening systems do not vary in strength, we can average the equivalent widths measured in epoch1 and epoch2. The MISC-COG analysis can be applied, because we detect many clear lines from these systems. Fig. 5 shows the best-fitting COGs for both intervening absorbers. We carry out the same approach as for the host, by first constraining b with the Fe II transitions. We find $b = 12.6^{+1.2}_{-1.4}$ km s^{-1} for int1 and $b = 20.6^{+5.7}_{-4.6}$ km s^{-1} for int2. The equivalent widths and the column densities of each ion species are listed in Table 3.

3.2 Detection and variability of transitions arising from excited levels of Fe II and Ni II

At the redshift of the host galaxy, we detect lines from fine-structure levels of Fe II (^{6}D$_{7/2}$, ^{6}D$_{5/2}$, ^{6}D$_{3/2}$ and ^{6}D$_{1/2}$) and metastable levels of Fe II (^{4}F$_{9/2}$ and ^{4}D$_{7/2}$) and Ni II (^{4}F$_{9/2}$). The equivalent width of many of these lines varies with time. This provides the opportunity to derive the distance between the burst location and the absorbing material, assuming that the population of these excited states is due to the UV radiation of the afterglow (see Section 3.2.1). With high-resolution spectra it would be possible to directly measure the column densities of the ions that are in the excited states, via Voigt profile fits to the fine-structure lines (see e.g. D'Elia et al. 2007; Vreeswijk et al. 2007). In order to obtain column densities from the equivalent widths, we need to take an intermediate step with the COG, where we fix b to the value found from the resonance Fe II lines (see Section 3.1.1), i.e. we assume that the ions in the excited states are in the same absorbing clouds as the ions in the ground state; for the implications of this assumption see the end of Section 3.2.1. Note that the value of b will only have a very small influence on the column densities of the excited ions, because the lines are all weak and lie mostly on the linear part of the COG.

Tables A1–A4 in Appendix A give an overview of all transitions from the fine-structure and metastable levels of Fe II and Ni II that would in principle be observable in the GMOS spectral range at this redshift. Due to the low spectral resolution, many of these lines are blended such that the individual variation of the components cannot be measured. The lines that are used in the modelling are shown in boldface in Tables A1–A4.

In order to obtain the column density $N_{\rm level}$ of ions in a specific excited state in an epoch, the equivalent widths of the transitions arising from this excited level are placed on the COG by assigning an $N_{\rm level}$ to this level. The best-fitting $N_{\rm level}$ is the value for which the ensemble of transitions fits the COG best (minimization of the χ^2). Figs 6 and 7 show the COG of the Ni II ^{4}F$_{9/2}$ and the Fe II ^{6}D$_{7/2}$ level per epoch (columns), together with the observed transitions from this level and Gaussian fits to the line profiles (rows). The best-fitting $N_{\rm level}$ and its errors are found with a Monte Carlo simulation, which we apply as follows. In every iteration, for each transition an equivalent width is randomly picked from a normal distribution with as mean the measured value and as sigma the measured error. For this simulated ensemble of equivalent widths, the best-fitting $N_{\rm level}$ is determined by minimizing the χ^2. After 10 000 iterations, the distribution of best-fitting $N_{\rm level}$'s is fitted with an asymmetric Gaussian (i.e. a normal distribution with a different σ on both sides), from which we derive the overall best $N_{\rm level}$ and its lower and upper 1σ error. Because the fine-structure lines lie mostly on the linear part of the COG, the effect of b is small, and the uncertainty of this value is not taken into account. If two or more transitions of a level

Table 3. The rest-frame equivalent widths W_λ for the lines from two intervening systems int1 and int2 at, respectively, $z_1 = 1.3147$ and $z_2 = 1.3179$. $\langle W_\lambda/\text{Å}\rangle$ is the weighted average of the rest-frame equivalent width (in Å) measured in GMOS epoch1 and epoch2. The COGs for the two systems are shown in Fig. 5. The column densities per ion species have been calculated with the COG with the best-fitting b; the errors on the column densities are the result of taking into account the range in b. Especially for lines on the flat part of the COG (e.g. Mg II), the effect on N due to b is large.

		int1 ($z_1 = 1.3147$) $b = 12.6^{+1.2}_{-1.4}$ km s^{-1}		int2 ($z_2 = 1.3179$) $b = 20.6^{+5.7}_{-4.6}$ km s^{-1}	
Line	f_λ	$\langle W_\lambda/\text{Å}\rangle$	$\log(N_{\rm ion}/{\rm cm}^{-2})$	$\langle W_\lambda/\text{Å}\rangle$	$\log(N_{\rm ion}/{\rm cm}^{-2})$
Al III 1854.7164	5.39×10^{-1}	0.053 ± 0.046	$12.74^{+0.29}_{-0.43}$	0.229 ± 0.049	$13.42^{+0.27}_{-0.17}$
Al III 1862.7895	2.68×10^{-1}	0.073 ± 0.047	–	0.171 ± 0.049	–
Fe II 2249.8754	2.190×10^{-3}	0.032 ± 0.036	$14.28^{+0.15}_{-0.09}$	[a]	
Fe II 2344.2129	1.252×10^{-1}	0.317 ± 0.030	–	0.176 ± 0.027	$13.57^{+0.09}_{-0.08}$
Fe II 2374.4604	3.297×10^{-2}	0.182 ± 0.028	–	0.034 ± 0.024	–
Fe II 2382.7641	3.432×10^{-1}	0.365 ± 0.030	–	0.325 ± 0.029	–
Fe II 2586.6495	7.094×10^{-2}	0.296 ± 0.027	–	0.136 ± 0.023	–
Fe II 2600.1722	2.422×10^{-1}	0.405 ± 0.028	–	0.344 ± 0.027	–
Mg II 2796.352	6.123×10^{-1}	0.532 ± 0.030	$14.86^{+0.26}_{-0.47}$	0.845 ± 0.035	$14.83^{+1.39}_{-0.68}$
Mg II 2803.531	3.054×10^{-1}	0.531 ± 0.030	–	0.792 ± 0.034	–
Mg I 2852.9642	1.83	0.143 ± 0.023	$12.17^{+0.09}_{-0.11}$	0.118 ± 0.022	$12.01^{+0.09}_{-0.11}$

[a]This line is blended with Ni II ^{4}F$_{9/2}$ λ2166.23 at the host redshift.

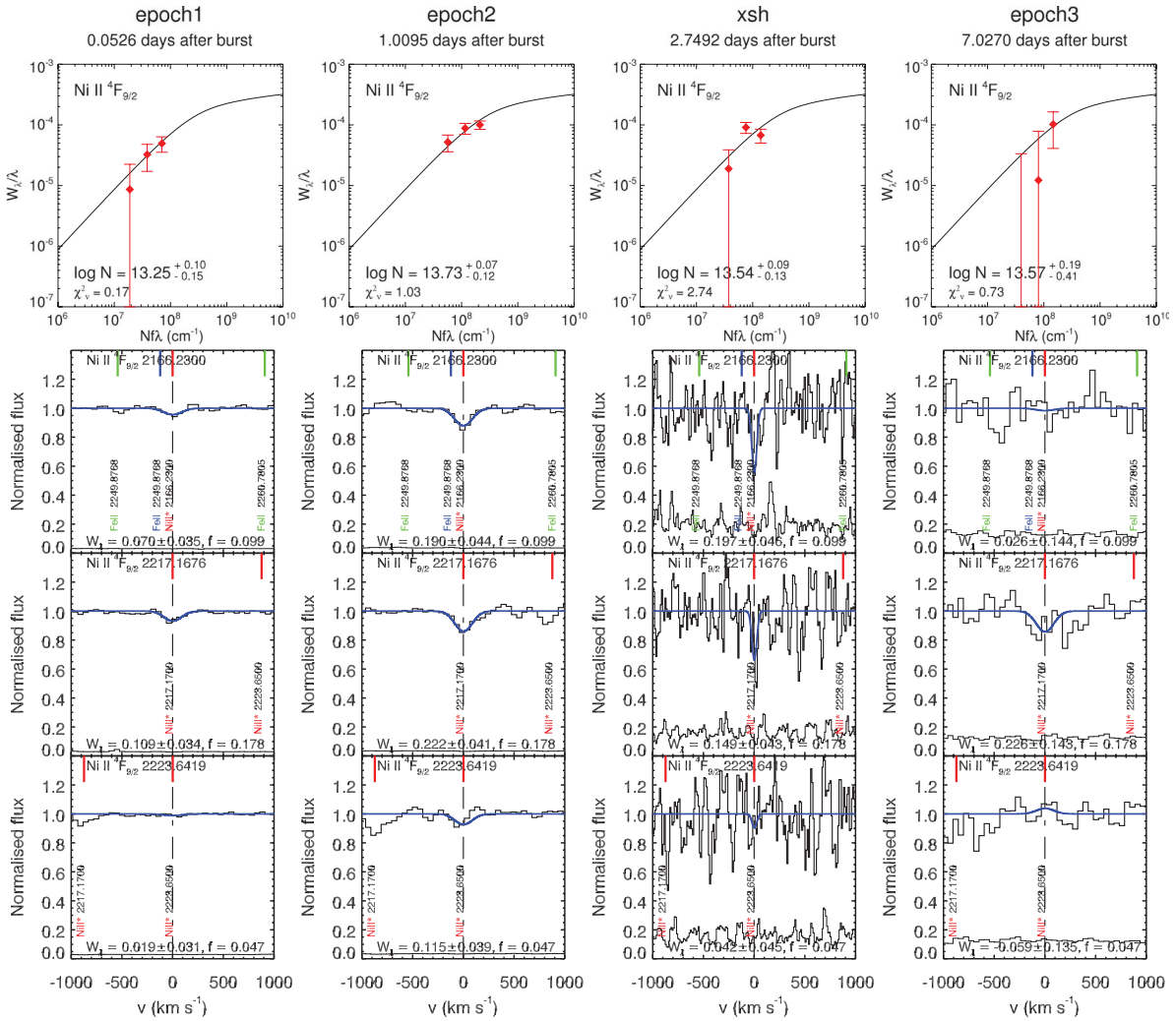

Figure 6. COGs and spectrum excerpts for the three detected lines from the Ni II $^4F_{9/2}$ metastable level. Every column represents an epoch, with the observed time since the burst indicated on top. The upper plot shows the COG for $b = 22.1$km s^{-1} to which we fit the equivalent widths for the three transitions (red diamonds). The best-fitting column density $N_{\rm level}$ is indicated, together with the χ^2_ν of the COG fit. Below the COG, the three individual lines are displayed on a velocity scale, with the corresponding Gaussian line profile fit. The rest-frame equivalent width and oscillator strength are indicated. We use the same line label colouring as in Fig. 1.

are detected in an epoch (i.e. if $|W_\lambda| > \sigma(W_\lambda)$), we obtain a value for $N_{\rm level}$, otherwise we obtain an upper limit (see Table 4).

3.2.1 UV-pumping models

The column densities of the fine-structure and metastable states are found to vary in time (see Table 4 and Fig. 8). The presence, and variation, of fine-structure lines in GRB afterglow spectra can generally well be explained by excitation due to the UV flux of the GRB afterglow. Prochaska et al. (2006) suggest that this is the dominant excitation mechanism, especially when variability is measured. The early high-resolution spectroscopic data obtained for GRB 060418 (Vreeswijk et al. 2007) allowed systematic tests of other excitation mechanisms such as a background IR field and collisional excitation, but these are ruled out with high confidence and the UV-pumping scenario is strongly favoured as the leading mechanism. For GRB 100901A we assume that UV pumping is the only relevant excitation mechanism.

We apply the photoexcitation model introduced by Vreeswijk et al. (2007, 2011, 2013). For technical details, we refer to the 2013 paper. The general idea is that the UV flux of the afterglow temporarily excites ions in a cloud with thickness l at a distance d from the location of the burst. As the afterglow brightness fades in time, the excited levels depopulate after a time which is determined by the Einstein coefficient A_{ul} or, equivalently, the oscillator strength of the transitions considered. For a given set of input parameters, the column density of each excited level as a function of time, $N_{\rm level}(t)$, is predicted by the model. By comparing this temporal behaviour to the measured $N_{\rm level}(t)$ for all levels simultaneously, we can optimize the parameters.

The afterglow flux is included as an interpolated series of R-band magnitudes[2] $m_R(t)$ (see the upper panel of Fig. 8), which corresponds to the rest-frame UV flux (at ∼2700 Å) responsible for populating the levels. The monochromatic flux in the host-galaxy rest

[2] The observed R-band magnitudes come from GCNs [Andreev et al. (2010a,b,c,d,e); Kuroda et al. (2010a,b); Volnova et al. (2010); assembled by Gomboc et al. (in preparation)].

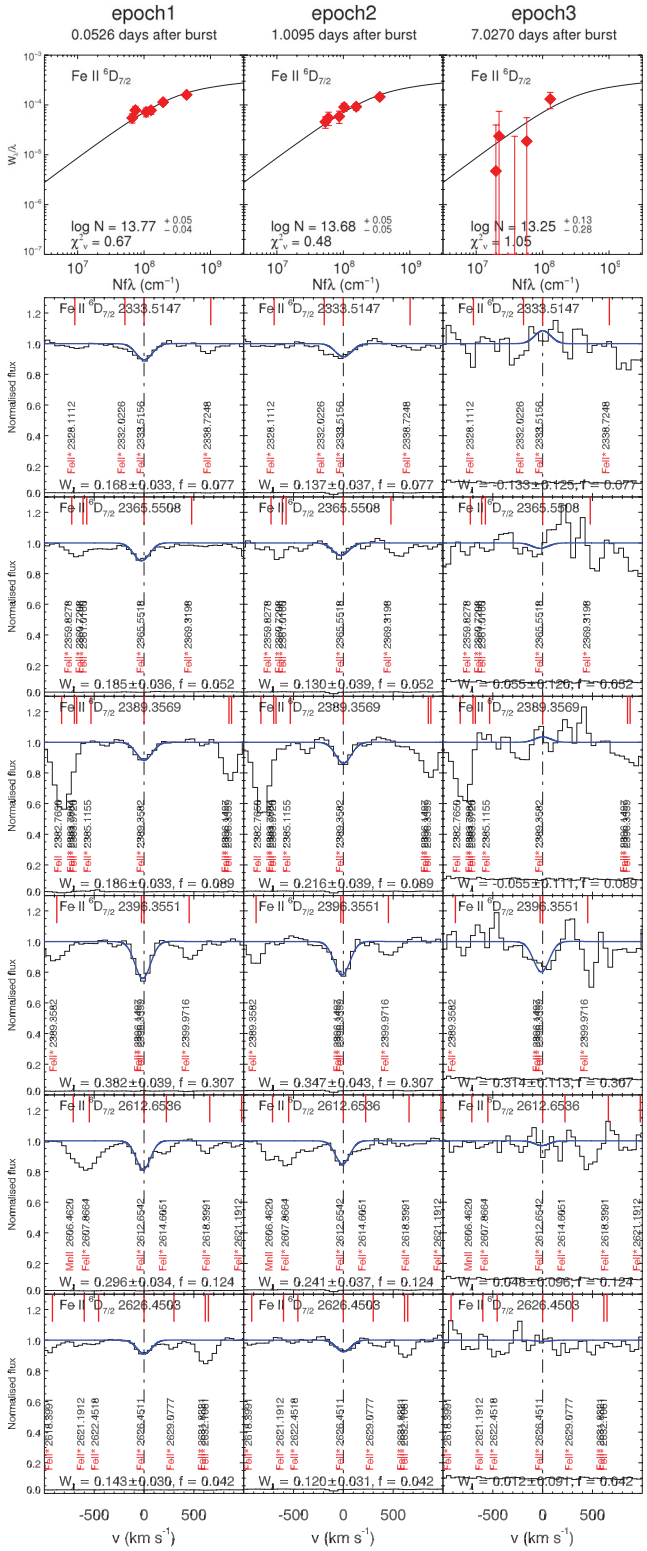

Figure 7. The same as Fig. 6, only for the six detected lines from the Fe II $^6D_{7/2}$ fine-structure level. We omit the xsh epoch, because for this level none of the lines was significantly detected due to the low S/N.

frame at the GRB-facing side of the absorbing cloud is computed as follows:

$$F_\nu^{\rm rest}(t) = \frac{F_0 \cdot 10^{[m_R(t) - A_{R,\rm gal}]/-2.5}}{1+z_{\rm h}} \left[\frac{\lambda_{\rm rest}(1+z_{\rm h})}{6415\,\text{Å}}\right]^{\beta_\nu} \left[\frac{D_{\rm L}}{d}\right]^2 \quad (3)$$

in which $F_0 = 3.02 \times 10^{-20}$ erg s^{-1} cm^{-2} Hz^{-1} is the flux of Vega at the effective wavelength (6410 Å) of the R band (Fukugita, Shimasaku & Ichikawa 1995), $A_{R,\rm gal} = 0.264$ is the Galactic extinction (Schlegel, Finkbeiner & Davis 1998), $\lambda_{\rm rest}$ is the wavelength array of the relevant transitions at which the flux is required to calculate the amount of excitation, β_ν is the spectral slope and $D_{\rm L} = 9.968 \times 10^9$ pc is the luminosity distance. The effective Doppler parameter b is fixed to 22.1 km s^{-1}, consistent with how we converted equivalent widths to column densities (see Section 3.2). Parameters that can be constrained from the light curve and/or SED fitting (Gomboc et al., in preparation) are kept fixed: optical spectral slope $\beta_\nu = 0.82$, and optical extinction in the host galaxy $A_V = 0.21$ assuming a Small Magellanic Cloud extinction profile (Gomboc et al., in preparation). We performed models with $A_V = 0$ as well to study the effect. A_V is not included in equation (3) because the model allows us to specify where the optical extinction takes place. We place the extinction in the absorbing cloud and apply the necessary corrections to the flux.

Table 5 shows the fit results of the model to the measured $N_{\rm level}(t)$ as listed in Table 4, with different requirements for the parameters. The model without extinction fits the data best with a small cloud at ∼250 pc, but when we include optical extinction $A_V = 0.2$, the data favour a configuration with a very large (>1 kpc) absorbing cloud at a smaller distance. Fixing the cloud size l leads to absorber distances of $d \sim$ 165–275 pc. Fig. 8 shows the fit to the data for the model with $l \leq 500$ pc (solid lines) and the model with $l = 1$ pc (dotted lines). Both models are decent fits: our data are not constraining enough to discriminate between the close large and the distant small cloud case. But in all cases, the influence of the GRB reaches distances of a few hundreds of parsecs. In Section 4.1 we will discuss the implications of this estimated absorber distance and compare it to values found in other GRBs.

Though not detectable with the spectral resolution used, it could be possible that the ground-state Fe II is present in more velocity components than excited Fe II, i.e. that there is Fe II that is not associated with the excited gas. If there exists more Fe II further away, then this would decrease the amount of Fe II that is associated with the excited Fe II, and hence this would move the absorber closer to the burst, i.e. we would infer a smaller GRB–absorber distance. Very roughly, if this fraction of Fe II associated with excited Fe II is only 50 per cent (rather than the now assumed 100 per cent), then it would decrease the distance by a factor of $\sqrt{2}$. So even assuming that such a large fraction (50 per cent) of the ground-state Fe II is further away does not change the inferred distance much.

3.2.2 *Atomic data*

In the full analysis from the COG to the photoexcitation model fitting, we need to adopt a set of values for vacuum wavelengths λ and oscillator strengths f_λ. The results of the analysis described in this paper are obtained with the atomic data given in Tables A1–A4. This atomic parameter set is the same as the one used in CLOUDY (Ferland et al. 1998), a widely used photoionization code, and comes from Verner et al. (1999) and references therein (see also Ledoux et al. 2009). The choice for this set is in principle arbitrary, but chosen such that our results can easily be compared with other works on GRB afterglow spectra. We tested the dependence of our results on this input by carrying out the full analysis with a different set of values for λ and f_λ. This alternative set is the same as used

Table 4. Lower level column densities $\log(N_{\rm level}(t)/{\rm cm}^{-2})$ for Fe II and Ni II excited states derived from fine-structure line equivalent widths with the COG analysis. All errors and limits are 1σ.

		Fe II						Ni II
	Time (d)	$^6D_{9/2}$	$^6D_{7/2}$	$^6D_{5/2}$	$^6D_{3/2}$	$^6D_{1/2}$	$^4D_{7/2}$	$^4F_{9/2}$
epoch1	0.0526	$15.20^{+0.08}_{-0.09}$	$13.77^{+0.05}_{-0.04}$	$13.58^{+0.06}_{-0.10}$	$13.30^{+0.07}_{-0.09}$	$12.92^{+0.11}_{-0.14}$	$12.54^{+0.11}_{-0.18}$	$13.25^{+0.10}_{-0.15}$
epoch2	1.0095	$15.29^{+0.07}_{-0.10}$	$13.68^{+0.05}_{-0.05}$	$13.46^{+0.09}_{-0.13}$	$13.14^{+0.09}_{-0.15}$	<12.83	$12.54^{+0.11}_{-0.24}$	$13.73^{+0.07}_{-0.12}$
xsh	2.7492	$15.16^{+0.12}_{-0.18}$	<13.46	<14.02	<13.47	<13.40	<13.03	$13.54^{+0.09}_{-0.13}$
epoch3	7.0270	$15.34^{+0.21}_{-0.48}$	<13.37	<13.80	<13.39	<13.47	<12.97	<13.75

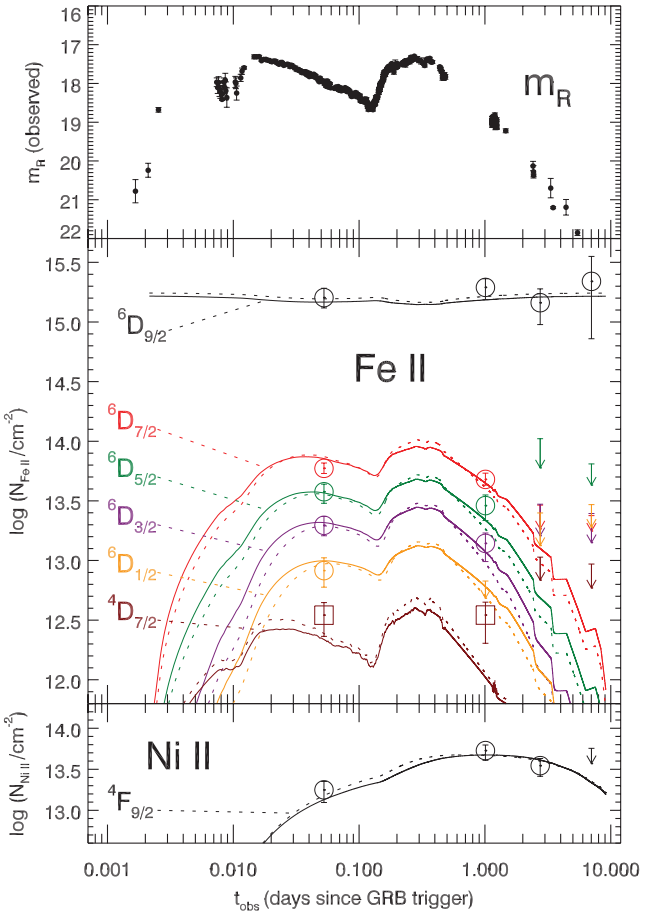

Figure 8. Top panel: observed *R*-band magnitudes from various observatories (see the text), which are used as input for the photoexcitation model (see Section 3.2.1). Middle and bottom panels: column density as a function of the observed time for Fe II fine-structure and metastable levels, and for the Ni II $^4F_{9/2}$ metastable level. The open circles and squares (arrows) indicate the column densities (limits) derived for each excited state (see Table 4). The solid lines denote the predicted best-fitting result of the photoexcitation model with a maximum absorber thickness of $l \leq 500$ pc ($\chi^2_\nu = 1.15$), the dotted line for a model with a fixed absorber thickness of $l = 1$ pc ($\chi^2_\nu = 1.35$), both with $A_V = 0.21$.

in Vreeswijk et al. (2007) and uses atomic data from Quinet, Le Dourneuf & Zeippen (1996), Morton (2003) and Kurucz (2003). This leads to a 2 per cent lower *b*, and differences up to 0.06 dex in $\log N(t)$. The final resulting *l* and *d* of the cloud from the modelling in Section 3.2.1 differ by <10 per cent, sometimes with lower values for χ^2_ν. The latter fact is, however, not a reason to adopt the alternative set but rather to interpret the scatter in the results as an additional error.

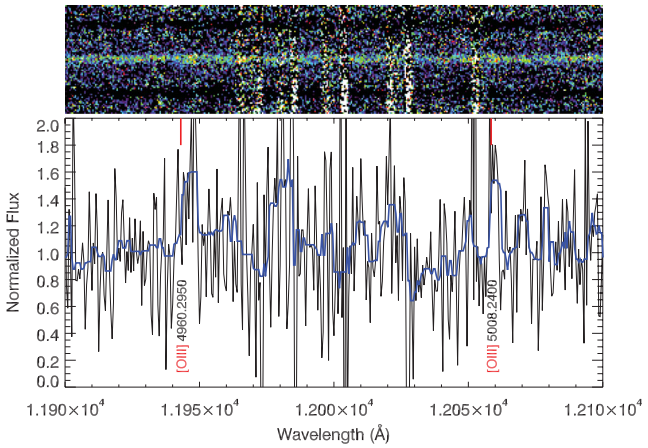

Figure 9. [O III] host emission lines, redshifted to $\sim 1.2\mu$ in the xsh-NIR spectrum. The top panel shows the 2D spectrum (0.5 Å pixel^{-1}). The bottom panel shows in black the normalized 1D spectrum (0.5 Å pixel^{-1}); in blue the same spectrum, but with a 10 pixel median filter to make the lines easier to see. The non-identified peaks in the 1D spectrum are due to residuals of skyline subtraction which are visible in the 2D spectrum as vertical white strips.

3.3 Emission lines

Because GRBs originate in star-forming galaxies, we have searched for emission lines at the host-galaxy redshift. There is tentative evidence for [O III] λ5007 (see Fig. 9), of which we estimate the flux to be $4.2 \pm 1.3 \times 10^{-17}$ ergs^{-1}cm^{-2}, an error including systematics due to flux calibration. [O III] λ4959 appears to be present, but is blended with a nearby skyline and cannot be measured. We do not detect Hα, Hβ or [O II] due to low S/N and/or skyline blends.

4 DISCUSSION

We have shown that the GRB 100901A afterglow UV radiation excited Fe II and Ni II ions in an absorbing cloud located a few hundred parsecs away in the host-galaxy ISM (Section 3.2). The ionic column densities we derive for the part of this host galaxy that is along the line of sight (Section 3.1) are very comparable to other GRB hosts where fine-structure lines are detected in the afterglow spectra (see e.g. Penprase et al. 2006; Prochaska et al. 2006; Vreeswijk et al. 2007; D'Elia et al. 2009b). Furthermore, the part of the galaxy we probe does not appear to be a special case in the context of dust depletion (Section 3.1.1). Modelling of the variation of the lines from the excited states allows us to estimate the distance to, and the size of, the absorbing cloud. This has been possible for about a dozen of bursts; in the following section we will discuss what these absorber distances teach us about the use of GRB afterglows as probes of galaxies.

Table 5. Photoexcitation modelling results for the environment of GRB 100901A with different settings. Column (1) lists extinction A_V in the host galaxy, (2) requirement for the distance d from the burst to the absorber, (3) requirement for the thickness l of the absorbing cloud, (4) fit result d, (5) fit result l, (6) pre-burst column densities of Fe II and (7) Ni II (ground state) and (8) the reduced chi-square of the fit. See also Fig. 8.

Input A_V	d	l	Output d (pc)	l (pc)	$\log\left(N_{\rm Fe\,II}/{\rm cm}^{-2}\right)$	$\log\left(N_{\rm Ni\,II}/{\rm cm}^{-2}\right)$	χ^2_ν
0.0	Free	Free	250 ± 75	0^{+240}_{-}	$15.25^{+0.05}_{-0.05}$	$13.91^{+0.07}_{-0.08}$	1.54
0.2	Minimal 100 pc	Free	100^{+61}_{-}	1127 ± 569	$15.26^{+0.05}_{-0.06}$	$14.14^{+0.10}_{-0.13}$	0.73
0.2	Free	Fixed to 1 pc	275 ± 12	1	$15.24^{+0.05}_{-0.06}$	$13.94^{+0.06}_{-0.07}$	1.35
0.2	Free	Fixed to 100 pc	249 ± 13	100	$15.24^{+0.05}_{-0.06}$	$13.95^{+0.06}_{-0.07}$	1.33
0.2	Free	Maximal 500 pc	165 ± 73	500^{+}_{-469}	$15.22^{+0.05}_{-0.06}$	$14.02^{+0.10}_{-0.13}$	1.15

4.1 GRBs as probes of galaxies

GRB afterglows are used as probes of their host galaxies, making use of the fact that the afterglow can be extremely bright for a short time. An advantage (for example, over galaxies in QSO sight lines) is that afterglows select star-forming galaxies, under the generally accepted assumption that GRBs are linked to (massive) star formation (Woosley 1993; Paczyński 1998). In order to judge how useful they are as galaxy probes, it is important to understand what the influence of the GRB and its afterglow is on the environment, and what part of the host galaxy we are probing. For about a dozen of GRB afterglows (see Table 6), the distance between the region where the absorption lines originate and the site where the burst has gone off has been derived with spectroscopy. The typical absorber distance is of the order of a few hundred pc, so the values we find for GRB 100901A appear to be normal (Table 6). These values are also in agreement with lower limits on the absorber distance (>50–100 pc) revealed by the presence of Mg I absorption lines (Prochaska et al. 2006).

Evidently, a GRB is able to affect the ISM out to distances of 100–1000 pc, which can be much further out than only the star-forming region of the GRB progenitor. For example, the largest star-forming region in the Local Group, the Tarantula nebula, has a diameter of ∼200 pc (Lebouteiller et al. 2008). First, this means that the GRB and its afterglow could have considerably influenced the environment it probes. Secondly, the absorption lines that we observe are probably not from the immediate star-forming region of the progenitor of the burst. This is important, as many stellar evolution models that are proposed as long GRB progenitors critically rely on a low metallicity (in particular, iron group element abundances; see e.g. Woosley & Heger 2006). Knowing the distance to the abundance-providing cloud gives more quantitative input into the reliability of the found abundances as tracers of the progenitor abundances.

4.2 Can low-*R* spectra be of use in the analysis of fine-structure line variation?

Our analysis of the fine-structure line variability in GRB 100901A differs from other studies because it is predominantly based on low-resolution spectra, while most other absorber distances are determined from spectra with a 25–40 times higher spectral resolution (see Table 6). Low resolution allowed us to monitor the spectrum over a much longer time span. We note that GRB 100901A remained particularly bright even after a week. The combination of our observations and the excitation modelling shows that we detect the peak of the Ni II $^4F_{9/2}$ level population at around 1 d after the burst in the observer's frame (see Fig. 8), which to date has not been observed. The downside is that low-resolution spectroscopy yields less accurate results, because additional steps and assumptions are required to translate equivalent widths to column densities. Furthermore, it is difficult to disentangle different velocity components, limiting the degree to which we can map the internal dynamical structure of the host galaxy.

When a (multi-epoch) low-resolution data set is available, we have shown that it is worthwhile to measure the variation and estimate the absorber distance by fitting a photoexcitation model to it. Especially the lines from the Ni II $^4F_{9/2}$ metastable level have proven to be useful for these kinds of long time-span spectroscopic data sets. These lines are strong, relatively isolated from other common lines in the spectrum, but still close to each other (with GMOS, one would be able to catch all four of them if the burst is at $0.8 < z < 1.9$), and it takes longer for the levels to depopulate compared to the Fe II fine-structure levels. In terms of recommendations for observing strategies, it would still be most useful to obtain a high-resolution spectrum as soon as possible after the burst, but a late-time (after a few days depending on the brightness) spectroscopic follow-up at low resolution can provide additional constraints on the line variation. The information about the different velocity components and their Doppler parameters obtained from the earliest spectrum can be used to interpret the late-time low-resolution data more accurately.

5 SUMMARY AND CONCLUSIONS

We have analysed the optical to NIR spectra of the afterglow of GRB 100901A. Our data set consists of three low-resolution spectra obtained with Gemini-N/GMOS at 1 h, 1 d and 7 d after the burst, and one medium-resolution VLT/X-shooter spectrum taken nearly 3 d post burst. At a redshift of 1.4084 a wealth of metal resonance and fine-structure lines is detected, allowing us to estimate column densities of Fe, Si, Cr, Mn, Zn, Mg, Ca and Al with an MISC-COG analysis. The obtained metal column densities are similar to what has been found in many GRB sight lines. Lyman α is not detected, so no metallicity can be determined.

$[{\rm Fe/Zn}] = -1.13 \pm 0.10$ suggests the presence of dust in the host galaxy. A comparison of the observed dust depletion pattern with sight lines in the MW (Savage & Sembach 1996) reveals a slight preference for a WH-like depletion pattern.

The spectrum shows two intervening absorbers at redshifts 1.3147 and 1.3179. Lines of Fe II, Al II, Al III, Mg I and Mg II have been detected and the corresponding column densities are estimated with the MISC-COG technique. We do not see significant variation in the strength of any of these lines from the intervening absorbers. Under simple assumptions for the projected source size as a function of time, this lack of variability sets a lower limit of 0.03 pc

Table 6. Bursts for which an absorber distance has been derived from (the variability of) lines from excited and/or ionized states in the afterglow spectrum. Column (1) lists burst ID, (2) number of epochs, (3) approximate time (observer's frame) between the different epochs, (4) telescope and spectrograph with which the data have been taken, (5) and (6) the ions and levels/lines for which variability is measured and/or modelled, (7) redshift of the burst, (8) neutral hydrogen column density, and (9) and (10) distance between the burst and the region where the lines originate, and the size of this region following from modelling of the variability, column (11) reference.

Burst	#	$\Delta t_{\rm obs}$	Instrument	Ion	Levels/lines	$z_{\rm h}$	$\log N_{\rm H\,I}$	d (pc)	l (pc)	Reference
020813	2	∼16 h	KECK/LRIS VLT/UVES	Fe II	$^6D_{7/2}$ λ2396	1.25	–	50−100	–	1
050730	2	∼1 h	VLT/UVES	Fe II	$^6D_{7/2}$, $^6D_{5/2}$,$^6D_{3/2}$,$^6D_{1/2}$, $^4F_{9/2}$, $^4F_{7/2}$,$^4F_{5/2}$,$^4F_{3/2}$, $^4D_{7/2}$, $^4D_{5/2}$	3.97	22.10	124 ± 20	147^{+68}_{-54}	2, 3, 4
051111	1		KECK/HIRES	Fe II Si II	$^6D_{7/2}$, $^6D_{5/2}$,$^6D_{3/2}$,$^6D_{1/2}$, $^2P^{\circ}_{3/2}$	1.55	–	a few times 10^2	–	5, 6
060206	2[a]		WHT/ISIS	Si II O I C II	$^2P^{\circ}_{3/2}$, $^3P^{\circ}_0$, $^3P^{\circ}_1$, $^2P^{\circ}_{3/2}$	4.05	20.85 ± 0.1	$\sim 10^3$	–	7, 8
060418	6	5−30 min	VLT/UVES	Fe II Ni II	$^6D_{7/2}$, $^6D_{5/2}$,$^6D_{3/2}$,$^6D_{1/2}$, $^4F_{9/2}$, $^4D_{7/2}$, $^4F_{9/2}$	1.49	–	480 ± 56	–	3, 9
080310	2−4	10−20 min	VLT/UVES	Fe II Fe III Si II C II	$^6D_{7/2}$, $^6D_{5/2}$,$^6D_{3/2}$,$^6D_{1/2}$, $^4F_{9/2}$, $^4D_{7/2}$, ^5D, $^7S_3$, $^2P^{\circ}_{3/2}$, $^2P^{\circ}_{3/2}$	2.43	18.70 ± 0.1	200−400	0−100	10, 11
080319B	3	40−60 min	VLT/UVES	Fe II	$^6D_{7/2}$, $^6D_{5/2}$,$^6D_{3/2}$,$^6D_{1/2}$, $^4F_{9/2}$, $^4F_{7/2}$, $^4D_{7/2}$, $^4D_{5/2}$,	0.94	–	560−1700	–	3, 12
080330	1		VLT/UVES	Fe II Si II Ni II	$^6D_{7/2}$, $^6D_{5/2}$,$^6D_{3/2}$,$^6D_{1/2}$, $^4F_{9/2}$, $^2P^{\circ}_{3/2}$, $^4F_{9/2}$	1.51	–	79^{+11}_{-14}	–	3, 13
081008	4[a]	7−25 min	VLT/UVES VLT/FORS2	Fe II Si II Ni II	$^6D_{7/2}$, $^6D_{5/2}$,$^6D_{3/2}$, $^4F_{9/2}$, $^4D_{7/2}$, $^2P^{\circ}_{3/2}$, $^4F_{9/2}$	1.97	21.11 ± 0.10	52 ± 6 and 200^{+60}_{-80}	–	14
090926	4[a]		VLT/X-shooter	Fe II Si II O I C II Ni II	$^6D_{7/2}$, $^4F_{9/2}$, $^2P^{\circ}_{3/2}$, $^3P^{\circ}_0$, $^3P^{\circ}_1$, $^2P^{\circ}_{3/2}$, $^4F_{9/2}$	2.11	21.60 ± 0.07	677 ± 42 and 5×10^3	–	3, 15
100219A	1		VLT/X-shooter	Si II	$^2P^{\circ}_{3/2}$	4.67	21.14 ± 0.15	300 and 10^3		16
100901A	4	1 h–1 week	Gemini-N/GMOS VLT/X-shooter	Fe II Ni II	$^6D_{7/2}$, $^6D_{5/2}$,$^6D_{3/2}$,$^6D_{1/2}$, $^4D_{7/2}$, $^4F_{9/2}$	1.41	–	a few times 10^2	1−1000	17

[a]More than one epoch is obtained, but the distance measurement did not follow from modelling the variation.

References: (1) Dessauges-Zavadsky et al. (2006); (2) Ledoux et al. (2009); (3) Vreeswijk et al. (2011); (4) D'Elia et al. (2007); (5) Penprase et al. (2006); (6) Prochaska et al. (2006); (7) Fynbo et al. (2006); (8) Thöne et al. (2008); (9) Vreeswijk et al. (2007); (10) De Cia et al. (2012); (11) Vreeswijk et al. (2013); (12) D'Elia et al. (2009a); (13) D'Elia et al. (2009b); (14) D'Elia et al. (2011); (15) D'Elia et al. (2010b); (16) Thöne et al. (2011); (17) this work.

on the size (or homogeneity scale) of the absorbing clouds in these foreground galaxies.

At the host-galaxy redshift we detect lines arising from fine-structure levels of the ground state of Fe II and metastable levels of Fe II and Ni II. The strengths of these lines are found to vary significantly in time. By grouping transitions that arise from the same lower level, we have used the COG from the Fe II resonance lines to retrieve the temporal behaviour of the column density of each of these excited ion species. This information is fed into a photoexcitation model, that uses the rest-frame UV flux of the burst as input. We assume that the excited levels are populated due to the UV radiation produced by the afterglow. The model computes the distance between the burst location and the cloud of gas in which the lines originate, and the size of this cloud. For GRB 100901A, we estimate an absorber distance of a few hundred pc, which appears to be typical compared with similar studies.

This is the first time that a fine-structure line variability analysis is predominantly based on low-resolution spectra, and as a consequence of that, also the longest time span over which such variation is detected and modelled. The decrease of the Ni II $^4F_{9/2}$ metastable level population has not been detected before; our data, in combination with our modelling results, show that we cover the peak of the excitation of this level. We argue that applying the fine-structure variability model to low-resolution data can yield a sensible estimate for the absorber distance, but additional intermediate steps (such as the COG) are necessary, which may cause additional (systematic) errors.

ACKNOWLEDGEMENTS

This research is partly based on observations obtained at the Gemini Observatory, which is operated by the Association Research in Astronomy, Inc., under a cooperative agreement with the NSF on behalf of the Gemini partnership.

The anonymous referee is thanked for useful suggestions that helped to significantly improve the paper. We thank H. J. van Eerten for useful discussion on the evolving source size of GRBs, and A. J. J. Raassen for a clear introduction to electron configurations, their notations and nomenclature.

OEH acknowledges the Dutch Research School for Astronomy (NOVA) for a PhD grant. JPUF acknowledges support from the ERC-StG grant EGGS-278202. The Dark Cosmology Centre is funded by the DNRF.

AG acknowledges funding from the Slovenian Research Agency and from the Centre of Excellence for Space Sciences and Technologies SPACE-SI, an operation partly financed by the European Union, European Regional Development Fund and Republic of Slovenia, Ministry of Higher Education, Science and Technology.

AP is grateful for support of the RFBR grants 12-02-01336-a and 11-01-92202-Mong-a.

RAMJ acknowledges support from the ERC via Advanced Investigator Grant no. 247295.

REFERENCES

Andreev M., Sergeev A., Pozanenko A., 2010a, GCN Circ., 11166, 1
Andreev M., Sergeev A., Pozanenko A., 2010b, GCN Circ., 11168, 1
Andreev M., Sergeev A., Pozanenko A., 2010c, GCN Circ., 11191, 1
Andreev M., Sergeev A., Pozanenko A., Parakhin N., Velichko S., Borachok N., Petkov V., 2010d, GCN Circ., 11200, 1
Andreev M., Sergeev A., Pozanenko A., 2010e, GCN Circ., 11201, 1
Asplund M., Grevesse N., Sauval A. J., Scott P., 2009, ARA&A, 47, 481
Balashev S. A., Petitjean P., Ivanchik A. V., Ledoux C., Srianand R., Noterdaeme P., Varshalovich D. A., 2011, MNRAS, 418, 357
Berger E., Penprase B. E., Cenko S. B., Kulkarni S. R., Fox D. B., Steidel C. C., Reddy N. A., 2006, ApJ, 642, 979
Bergeson S. D., Lawler J. E., 1993a, ApJ, 414, L137
Bergeson S. D., Lawler J. E., 1993b, ApJ, 408, 382
Bohlin R. C., Savage B. D., Drake J. F., 1978, ApJ, 224, 132
Chornock R., Berger E., Fox D., Levan A. J., Tanvir N. R., Wiersema K., 2010, GCN Circ., 11164, 1
Cucchiara A., Jones T., Charlton J. C., Fox D. B., Einsig D., Narayanan A., 2009, ApJ, 697, 345
Cucchiara A. et al., 2012, e-print (arXiv:1211.6528)
D'Elia V. et al., 2007, A&A, 467, 629
D'Elia V. et al., 2009a, ApJ, 694, 332
D'Elia V. et al., 2009b, A&A, 503, 437
D'Elia V. et al., 2010a, MNRAS, 401, 385
D'Elia V. et al., 2010b, A&A, 523, A36
D'Elia V., Campana S., Covino S., D'Avanzo P., Piranomonte S., Tagliaferri G., 2011, MNRAS, 418, 680
D'Odorico S. et al., 2006, Proc. SPIE, 626933
De Cia A. et al., 2012, A&A, 545, A64
de Ugarte Postigo A., Thöne C. C., Goldoni P., Fynbo J. P. U. the X-shooter GRB collaboration, 2011, Astron. Nachr., 332, 297
de Ugarte Postigo A. et al., 2012, A&A, 548, A11
Dessauges-Zavadsky M., Chen H.-W., Prochaska J. X., Bloom J. S., Barth A. J., 2006, ApJ, 648, L89
Elíasdóttir Á. et al., 2009, ApJ, 697, 1725
Ellison S. L., Ibata R., Pettini M., Lewis G. F., Aracil B., Petitjean P., Srianand R., 2004, A&A, 414, 79
Ferland G. J., Korista K. T., Verner D. A., Ferguson J. W., Kingdon J. B., Verner E. M., 1998, PASP, 110, 761
Fiore F. et al., 2005, ApJ, 624, 853
Fukugita M., Shimasaku K., Ichikawa T., 1995, PASP, 107, 945
Fynbo J. P. U. et al., 2002, in Gilfanov M., Sunyeav R., Churazov E., eds, Proc. MPA/ESO/MPE/USM Joint Astron. Conf., Lighthouses of the Universe: The Most Luminous Celestial Objects and Their Use for Cosmology, ESO, Springer-Verlag, Berlin, p. 187
Fynbo J. P. U. et al., 2006, A&A, 451, L47
Fynbo J. P. U. et al., 2009, ApJS, 185, 526
Goldoni P., Royer F., François P., Horrobin M., Blanc G., Vernet J., Modigliani A., Larsen J., 2006, Proc. SPIE, 6269K
Gorbovskoy E. S. et al., 2012, MNRAS, 421, 1874
Granot J., Piran T., Sari R., 1999, ApJ, 513, 679
Guidorzi C., Cano Z., Melandri A., Kopac D., 2010, GCN Circ., 11160, 1
Hjorth J. et al., 2012, APJ, 756, 187
Immler S. et al., 2010, GCN Circ., 11159, 1
Jenkins E. B., 1986, ApJ, 304, 739
Kuroda D., Hanayama H., Miyaji T., Watanabe J., Yanagisawa K., Yoshida M., Ohta K., Kawai N., 2010a, GCN Circ., 11205, 1
Kuroda D., Yanagisawa K., Shimizu Y., Toda H., Nagayama S., Yoshida M., Ohta K., Kawai N., 2010b, GCN Circ., 11172, 1
Kurucz R. L., 2003, in Piskunov N., Weiss W. W., Gray D. F., eds, Proc. IAU Symp. 210, Modelling of Stellar Atmospheres, Astron. Soc. Pac., San Francisco, p. 45
Lebouteiller V., Bernard-Salas J., Brandl B., Whelan D. G., Wu Y., Charmandaris V., Devost D., Houck J. R., 2008, ApJ, 680, 398
Ledoux C., Vreeswijk P. M., Smette A., Fox A. J., Petitjean P., Ellison S. L., Fynbo J. P. U., Savaglio S., 2009, A&A, 506, 661
Lu L., Sargent W. L. W., Barlow T. A., Churchill C. W., Vogt S. S., 1996, ApJS, 107, 475
Modigliani A. et al., 2010, Proc. SPIE, 773728
Morton D. C., 1991, ApJS, 77, 119
Morton D. C., 2003, ApJS, 149, 205
Paczyński B., 1998, ApJ, 494, L45
Penprase B. E. et al., 2006, ApJ, 646, 358
Petitjean P., Aracil B., Srianand R., Ibata R., 2000, A&A, 359, 457
Pettini M., Ellison S. L., Steidel C. C., Bowen D. V., 1999, ApJ, 510, 576
Pettini M., Ellison S. L., Steidel C. C., Shapley A. E., Bowen D. V., 2000, ApJ, 532, 65
Prochaska J. X., 2006, ApJ, 650, 272
Prochaska J. X., Wolfe A. M., 1996, ApJ, 470, 403
Prochaska J. X., Wolfe A. M., 1997, ApJ, 474, 140
Prochaska J. X., Wolfe A. M., 2000, ApJ, 533, L5
Prochaska J. X. et al., 2001, ApJS, 137, 21
Prochaska J. X., Chen H., Bloom J. S., 2006, ApJ, 648, 95
Prochaska J. X., Chen H., Dessauges-Zavadsky M., Bloom J. S., 2007, ApJ, 666, 267
Prochter G. E. et al., 2006, ApJ, 648, L93
Quinet P., Le Dourneuf M., Zeippen C. J., 1996, A&AS, 120, 361
Sakamoto T. et al., 2010, GCN Circ., 11169, 1
Savage B. D., Sembach K. R., 1996, ARA&A, 34, 279
Savaglio S., 2006, New J. Phys., 8, 195
Savaglio S., 2012, Astron. Nachr., 333, 480
Savaglio S., Fall S. M., 2004, ApJ, 614, 293
Savaglio S., Fall S. M., Fiore F., 2003, ApJ, 585, 638
Savaglio S., Glazebrook K., Le Borgne D., 2009, ApJ, 691, 182
Schady P., Savaglio S., Krühler T., Greiner J., Rau A., 2011, A&A, 525, A113
Schlegel D. J., Finkbeiner D. P., Davis M., 1998, ApJ, 500, 525
Spitzer L., 1978, Physical Processes in the Interstellar Medium. Wiley-Interscience, New York, p. 333
Thöne C. C. et al., 2008, A&A, 489, 37
Thöne C. C., Fynbo J., Goldoni P., de Ugarte Postigo A., Covino S., Campana S., and X-shooter GRB Collaboration, 2011, Astron. Nachr., 332, 281
Umeda H., Nomoto K., 2002, ApJ, 565, 385
Vacca W. D., Cushing M. C., Rayner J. T., 2003, PASP, 115, 389
van Paradijs J. et al., 1997, Nat, 386, 686
Vergani S. D., Petitjean P., Ledoux C., Vreeswijk P., Smette A., Meurs E. J. A., 2009, A&A, 503, 771
Verner D. A., Ferland G. J., Korista K. T., Yakovlev D. G., 1996, ApJ, 465, 487

Verner E. M., Verner D. A., Korista K. T., Ferguson J. W., Hamann F., Ferland G. J., 1999, ApJS, 120, 101
Vernet J. et al., 2011, A&A, 536, A105
Volnova A., Pozanenko A. E. K., Korobtsev I., 2010, GCN Circ., 11270, 1
Vreeswijk P. M. et al., 2001, ApJ, 546, 672
Vreeswijk P. M. et al., 2004, A&A, 419, 927
Vreeswijk P. M. et al., 2007, A&A, 468, 83
Vreeswijk P. M. et al., 2011, A&A, 532, C3
Vreeswijk P. M. et al., 2013, A&A, 549, A22
Watson D. et al., 2006, ApJ, 652, 1011
Wiersema K., 2011, MNRAS, 414, 2793
Wolfe A. M., Gawiser E., Prochaska J. X., 2005, ARA&A, 43, 861
Woosley S. E., 1993, ApJ, 405, 273
Woosley S. E., Heger A., 2006, ApJ, 637, 914

APPENDIX A: TABLES WITH LINE TRANSITIONS

Table A1. Lines from the ground state of Fe II (electron configurations $3d^6(^5D)4s - 3d^6(^5D)4p$) and its fine-structure levels, that could in principle be detected in the spectrum of GRB 100901A, because the transition would lie within the GMOS spectral range and the oscillator strength f_λ is not smaller than about 0.005 (except for the $^6D_{9/2}$ resonance lines). The lines of which the wavelengths are in boldface have been used in the modelling reported in Section 3.2. W_λ are measured equivalent widths per epoch, converted to the rest frame.

Lower level	λ_{vac} (Å)	f_λ	log gf	$J_i - J_k$	Terms	W_λ(epoch1)	W_λ(epoch2)	W_λ(xsh)	W_λ(epoch3)
$^6D_{9/2}$	1608.4509	0.053 99	−0.268	9/2 − 7/2	$a^6D - y^6P^\circ$	Possibly present, but blended with Al II λ1670 at $z = 1.318$.			
0 cm^{-1}	1611.2004	0.001 36	−1.867	9/2 − 7/2	$a^6D - z^4F^\circ$	Not detected.			
	2249.8754	0.002 19	−1.660	9/2 − 7/2	$a^6D - z^4D^\circ$	0.129 ± 0.034	0.151 ± 0.040	0.143 ± 0.044	0.093 ± 0.138
	2260.7793	0.002 62	−1.582	9/2 − 9/2	$a^6D - z^4F^\circ$	0.152 ± 0.034	0.168 ± 0.040	0.074 ± 0.060	0.256 ± 0.125
	2344.2129	0.125 23	0.098	9/2 − 7/2	$a^6D - z^6P^\circ$	0.748 ± 0.047[a]	0.798 ± 0.054[a]	0.704 ± 0.189[a]	0.557 ± 0.134[a]
	2374.4604	0.032 97	−0.482	9/2 − 9/2	$a^6D - z^6F^\circ$	0.590 ± 0.045	[b]	[b]	[b]
	2382.7641	0.343 21	0.536	9/2 − 11/2	$a^6D - z^6F^\circ$	0.683 ± 0.045	[b]	[b,c]	[b]
	2586.6495	0.070 94	−0.149	9/2 − 7/2	$a^6D - z^6D^\circ$	0.705 ± 0.043	0.727 ± 0.048	0.696 ± 0.145	0.629 ± 0.107
	2600.1722	0.242 26	0.384	9/2 − 11/2	$a^6D - z^6D^\circ$	0.780 ± 0.045	[b]	[b,c]	[b]
$^6D_{7/2}$	**2333.5147**	0.077 76	−0.206	7/2 − 5/2	$a^6D - z^6P^\circ$	0.168 ± 0.034	0.137 ± 0.038	0.051 ± 0.189	−0.134 ± 0.126
384.790 cm^{-1}	**2365.5508**	0.052 85	−0.374	7/2 − 7/2	$a^6D - z^6P^\circ$	0.185 ± 0.036	0.130 ± 0.039	0.008 ± 0.222	0.056 ± 0.120
	2383.7873	0.005 57	−1.351	7/2 − 5/2	$a^6D - z^6F^\circ$	0.087 ± 0.031	0.071 ± 0.034	[c]	0.054 ± 0.107
	2389.3569	0.089 87	−0.143	7/2 − 7/2	$a^6D - z^6F^\circ$	0.187 ± 0.033	0.216 ± 0.040	−0.085 ± 0.303	−0.056 ± 0.112
	2396.3551	0.307 79	0.391	7/2 − 9/2	$a^6D - z^6F^\circ$	0.383 ± 0.040[d]	0.348 ± 0.043[d]	0.170 ± 0.275[d]	0.314 ± 0.114[d]
	2599.1457	0.108 63	−0.061	7/2 − 5/2	$a^6D - z^DF^\circ$	0.190 ± 0.031	0.096 ± 0.030	[c]	−0.019 ± 0.096
	2612.6536	0.124 85	−0.001	7/2 − 7/2	$a^6D - z^6D^\circ$	0.297 ± 0.035	0.241 ± 0.037	0.012 ± 0.106	0.049 ± 0.096
	2626.4503	0.042 66	−0.467	7/2 − 9/2	$a^6D - z^6D^\circ$	0.144 ± 0.030	0.120 ± 0.031	0.095 ± 0.118	0.012 ± 0.092
$^6D_{5/2}$	**2328.1100**	0.037 60	−0.647	5/2 − 3/2	$a^6D - z^6P^\circ$	0.052 ± 0.031	0.031 ± 0.036	0.064 ± 0.235	0.082 ± 0.132
667.683 cm^{-1}	2349.0215	0.089 35	−0.271	5/2 − 5/2	$a^6D - z^6P^\circ$	0.204 ± 0.035[e]	0.196 ± 0.038[e]	0.081 ± 0.154[e]	−0.139 ± 0.114[e]
	2381.4877	0.037 98	−0.642	5/2 − 7/2	$a^6D - z^6P^\circ$	0.022 ± 0.027	−0.009 ± 0.033	[c]	−0.004 ± 0.111
	2396.1487	0.016 36	−1.008	5/2 − 3/2	$a^6D - z^6F^\circ$	blend with $^6D_{7/2}$λ2396.3551, which dominates.			
	2399.9718	0.125 22	−0.124	5/2 − 5/2	$a^6D - z^6F^\circ$	0.169 ± 0.032	0.163 ± 0.037	0.071 ± 0.255	0.221 ± 0.124
	2405.6173	0.251 03	0.178	5/2 − 7/2	$a^6D - z^6F^\circ$	0.254 ± 0.036[f]	0.203 ± 0.039[f]	0.005 ± 0.205[f]	−0.076 ± 0.102[f]
	2607.8658	0.123 04	−0.132	5/2 − 3/2	$a^6D - z^6D^\circ$	0.308 ± 0.040[g]	0.242 ± 0.043	0.083 ± 0.108	0.007 ± 0.131
	2618.3984	0.048 00	−0.541	5/2 − 5/2	$a^6D - z^6P^\circ$	0.112 ± 0.029	0.057 ± 0.031	0.127 ± 0.109	−0.038 ± 0.114
	2632.1077	0.082 40	−0.306	5/2 − 7/2	$a^6D - z^6D^\circ$	0.252 ± 0.033[h]	0.169 ± 0.035[g]	−0.015 ± 0.114[g]	0.086 ± 0.088[g]
$^6D_{3/2}$	**2338.7238**	0.098 40	−0.405	3/2 − 3/2	$a^6D - z^6P^\circ$	0.090 ± 0.032	0.057 ± 0.036	0.127 ± 0.174	0.062 ± 0.128
862.613 cm^{-1}	2359.8270	0.067 88	−0.566	3/2 − 5/2	$a^6D - z^6P^\circ$	Part of a strongly blended complex, with a contribution of an unidentified line.			
	2405.1626	0.027 84	−0.953	3/2 − 1/2	$a^6D - z^6F^\circ$	Blend with $^6D_{5/2}$λ2405.6173, which dominates.			
	2407.3934	0.159 88	−0.194	3/2 − 3/2	$a^6D - z^6F^\circ$	0.122 ± 0.032	0.078 ± 0.033	0.014 ± 0.199	0.014 ± 0.112
	2411.2522	0.219 67	−0.056	3/2 − 5/2	$a^6D - z^6F^\circ$	0.227 ± 0.035[i]	0.115 ± 0.037[i]	0.181 ± 0.170[i]	0.031 ± 0.089[i]
	2614.6047	0.110 18	−0.356	3/2 − 1/2	$a^6D - z^6D^\circ$	0.119 ± 0.029	0.091 ± 0.032	0.007 ± 0.105	0.055 ± 0.095
	2621.1906	0.003 64	−1.837	3/2 − 3/2	$a^6D - z^6D^\circ$	0.047 ± 0.028	−0.016 ± 0.032	0.035 ± 0.114	0.022 ± 0.084
	2631.8314	0.124 30	−0.303	3/2 − 5/2	$a^6D - z^6D^\circ$	Blended with $^6D_{5/2}$λ2632.1077, see there for the total W_λ.			
$^6D_{1/2}$	2344.9996	0.168 19	−0.473	1/2 − 3/2	$a^6D - z^6P^\circ$	Blended with $^6D_{9/2}$λ2344.214 and $^4F_{7/2}$λ2344.6789, see there for the total W_λ.			
977.053 cm^{-1}	2411.8009	0.225 00	−0.347	1/2 − 1/2	$a^6D - z^6F^\circ$	Blended with $^6D_{3/2}$λ2411.2522, see there for the total W_λ.			
	2414.0437	0.190 47	−0.419	1/2 − 3/2	$a^6D - z^6F^\circ$	0.060 ± 0.030	0.028 ± 0.034	−0.081 ± 0.159	0.073 ± 0.125
	2622.4513	0.054 54	−0.962	1/2 − 1/2	$a^6D - z^6D^\circ$	0.036 ± 0.025	0.024 ± 0.029	0.114 ± 0.109	0.116 ± 0.114
	2629.0769	0.174 51	−0.457	1/2 − 3/2	$a^6D - z^6D^\circ$	0.079 ± 0.027	0.033 ± 0.031	0.008 ± 0.172	0.119 ± 0.109

[a] Blended with lines from $^6D_{1/2}$ and $^4F_{7/2}$, total W_λ is reported.
[b] W_λ of this resonance line is kept fixed to the value obtained at the first epoch to see the possible variation of the (half-) blended fine-structure lines.
[c] The line (blend) is clearly saturated, and cannot be fitted with Gaussian (components) in the X-shooter spectrum.
[d] Blended with $^6D_{5/2}$λ2396.1487, but we assume that the contribution from this line to the total W_λ is negligible.
[e] Blended with $^4F_{9/2}$λ2348.8346, this is the total W_λ.
[f] Blended with $^6D_{3/2}$λ2405.1626, this is the total W_λ.
[g] Blended with Mn II λ2606, but this line's W_λ is fixed after the first epoch.
[h] Blended with $^6D_{3/2}$λ2631.8314, this is the total W_λ.
[i] Blended with $^6D_{1/2}$λ2411.8009, this is the total W_λ.

Table A2. The same as Table A1, only for the lines from the metastable states of Fe II with electron configuration $3p^6 3d^7$.

Lower level	λ_{vac} (Å)	f_λ	log gf	$J_i - J_k$	Terms	W_λ(epoch1)	W_λ(epoch2)	W_λ(xsh)	W_λ(epoch3)
$^4F_{9/2}$	1610.9234	0.009 14	−1.039	9/2 − 9/2	$a^4F - y^4G^\circ$	Not detected, hardly in range, noisy region.			
1872.567 cm^{-1}	1637.3998	0.014 18	−0.848	9/2 − 7/2	$a^4F - x^4D^\circ$	Not detected, noisy region with many possible lines.			
	1702.0453	0.053 16	−0.274	9/2 − 11/2	$a^4F - z^4G^\circ$	Possibly detected, but shifted and blended with Ni IIλ1703, noisy region.			
	2332.0235	0.017 87	−0.748	9/2 − 7/2	$a^4F - z^4F^\circ$	0.052 ± 0.029	0.085 ± 0.037	0.109 ± 0.199	0.103 ± 0.123
	2348.8346	0.036 53	−0.437	9/2 − 7/2	$a^4F - z^4D^\circ$	Blended with $^6D_{5/2}$λ2349.0215, see there for total W_λ.			
	2360.7213	0.022 89	−0.640	9/2 − 9/2	$a^4F - z^4F^\circ$	Part of a strongly blended complex, with a contribution of an unidentified line.			
$^4F_{7/2}$	1625.5231	0.024 81	−0.702	7/2 − 9/2	$a^4F - y^4G^\circ$	Not detected, noisy region.			
2430.097 cm^{-1}	2344.6790	0.016 69	−0.874	7/2 − 5/2	$a^4F - z^4F^\circ$	Blended with $^6D_{9/2}$λ2344.214 and $^6D_{1/2}$λ2344.9996, see there for the total W_λ.			
	2361.0161	0.030 53	−0.612	7/2 − 5/2	$a^4F - z^4D^\circ$	Part of a strongly blended complex, with a contribution of an unidentified line.			
	2380.0023	0.017 32	−0.858	7/2 − 7/2	$a^4F - z^4D^\circ$	Not detected.			
$^4F_{5/2}$	1633.9093	0.026 20	−0.803	5/2 − 7/2	$a^4F - y^4G^\circ$	Not detected, noisy region with many possible lines.			
2837.950 cm^{-1}	2369.3195	0.029 18	−0.757	5/2 − 3/2	$a^4F - z^4D^\circ$	Not detected.			
	2383.9718	0.022 15	−0.876	5/2 − 5/2	$a^4F - z^4D^\circ$	Blended with many lines including the saturated $^6D_{9/2}$λ2382.7641.			
$^4F_{3/2}$	2375.9188	0.035 12	−0.852	3/2 − 1/2	$a^4F - y^4D^\circ$	0.061 ± 0.034^j	0.066 ± 0.034^j	−0.147 ± 0.202^j	−0.079 ± 0.100^j
3117.461 cm^{-1}	2385.1148	0.023 11	−1.034	3/2 − 3/2	$a^4F - y^4D^\circ$	Not detected, close to complex blend.			

^{j}Half-blended with $^6D_{9/2}$λ2374.4604, whose W_λ is fixed from the first epoch.

Table A3. The same as Table A1, only for the lines from the metastable states of Fe II with electron configuration $3d^6(^5D)4s$.

Lower level	λ_{vac} (Å)	f_λ	log gf	$J_i - J_k$	Terms	W_λ(epoch1)	W_λ(epoch2)	W_λ(xsh)	W_λ(epoch3)
$^4D_{7/2}$	1635.4005	0.068 57	−0.261	7/2 − 5/2	$a^4D - x^4P^\circ$	Heavily blended, noisy region.			
7955.299 cm^{-1}	**2563.3039**	0.135 20	0.034	7/2 − 5/2	$a^4D - z^4P^\circ$	0.037 ± 0.027	0.064 ± 0.032	−0.052 ± 0.248	0.047 ± 0.110
	2715.2173	0.045 43	−0.440	7/2 − 5/2	$a^4D - z^4D^\circ$	Not detected.			
	2740.3577	0.251 07	0.303	7/2 − 7/2	$a^4D - z^4D^\circ$	0.056 ± 0.026	0.027 ± 0.029	0.018 ± 0.099	0.114 ± 0.094
	2756.5512	0.307 59	0.391	7/2 − 9/2	$a^4D - z^4F^\circ$	0.050 ± 0.025	0.056 ± 0.030	0.097 ± 0.114	−0.045 ± 0.104
$^4D_{5/2}$	1641.7631	0.047 42	−0.546	5/2 − 3/2	$a^4D - x^4P^\circ$	Blended, noisy region.			
8391.938 cm^{-1}	1647.1625	0.020 26	−0.915	5/2 − 5/2	$a^4D - x^4P^\circ$	Blended, noisy region.			
	2564.2441	0.093 32	−0.252	5/2 − 3/2	$a^4D - z^4P^\circ$	Not detected.			
	2592.3179	0.052 19	−0.504	5/2 − 5/2	$a^4D - z^4P^\circ$	Not detected.			
	2728.3467	0.068 90	−0.384	5/2 − 3/2	$a^4D - z^4D^\circ$	Not detected.			
	2747.7942	0.187 91	0.052	5/2 − 5/2	$a^4D - z^4D^\circ$	Part of strongly blended complex.			
	2750.1347	0.328 08	0.294	5/2 − 5/2	$a^4D - z^4F^\circ$	Blended with $^4D_{3/2}$λ2749.9938 and $^4D_{1/2}$λ2750.2989.			
$^4D_{3/2}$	2567.6820	0.056 84	−0.643	3/2 − 1/2	$a^4D - z^4P^\circ$	Not detected.			
8680.454 cm^{-1}	2583.3564	0.083 45	−0.477	3/2 − 3/2	$a^4D - z^4P^\circ$	Not detected.			
	2731.5431	0.029 64	−0.926	3/2 − 3/2	$a^4D - z^4F^\circ$	Not detected.			
	2737.7761	0.065 74	−0.580	3/2 − 1/2	$a^4D - z^4D^\circ$	Not detected.			
	2747.2958	0.354 75	0.152	3/2 − 5/2	$a^4D - z^4F^\circ$	Part of strongly blended complex.			
	2749.9938	0.134 92	−0.268	3/2 − 3/2	$a^4D - z^4D^\circ$	Blended with $^4D_{5/2}$λ2750.1344 and $^4D_{1/2}$λ2750.2988.			
$^4D_{1/2}$	2578.6940	0.123 62	−0.607	1/2 − 1/2	$a^4D - z^4P^\circ$	Not detected.			
8846.768 cm^{-1}	2744.0089	0.440 26	−0.055	1/2 − 3/2	$a^4D - z^4F^\circ$	Possibly detected, but half blended Mg Iλ2853 at $z = 1.315$.			
	2750.2989	0.120 21	−0.619	1/2 − 1/2	$a^4D - z^4D^\circ$	Blended with $^4D_{5/2}$λ2750.1347 and $^4D_{3/2}$λ2749.9938.			

Table A4. The same as Table A1, only for the lines from the metastable states of Ni II with electron configurations $3p^6 3d^8(^3F)4s$.

Lower level	λ_{vac} (Å)	f_λ	log gf	$J_i - J_k$	Terms	W_λ(epoch1)	W_λ(epoch2)	W_λ(xsh)	W_λ(epoch3)
$^4F_{9/2}$	**2166.2300**	0.099 90	0.000	9/2 − 9/2	$^4F - ^2F^\circ$	0.070 ± 0.035	0.191 ± 0.045	0.197 ± 0.046	0.026 ± 0.145
8393.90 cm^{-1}	**2217.1676**	0.178 65	0.252	9/2 − 11/2	$^4F - ^4G^\circ$	0.110 ± 0.035	0.222 ± 0.042	0.150 ± 0.043	0.227 ± 0.143
	2223.6419	0.047 89	−0.320	9/2 − 9/2	$^4F - ^4G^\circ$	0.019 ± 0.031	0.116 ± 0.039	0.042 ± 0.046	−0.060 ± 0.136
	2316.7481	0.110 73	0.044	9/2 − 7/2	$^4F - ^4D^\circ$	Blended with a skyline.			

This paper has been typeset from a TEX/LATEX file prepared by the author.